Surfaces and Interfaces 38 (2023) 102820

Contents lists available at ScienceDirect

Surfaces and Interfaces

journal homepage: www.sciencedirect.com/journal/surfaces-and-interfaces

Design, synthesis and investigating the interaction of novel s-triazine collector with pyrite surface: A DFT-D3+U and experimental studies

Peace P. Mkhonto [a,*], Xingrong Zhang [b,*], Liang Lu [b], Wei Xiong [b], Yangge Zhu [b], Long Han [b], Phuti E. Ngoepe [a]

[a] Materials Modelling Centre, University of Limpopo, Private Bag X1106, Sovenga 0727, South Africa
[b] State Key Laboratory of Mineral Processing, BGRIMM Technology Group, Beijing 102600, China

ARTICLE INFO

Keywords:
DFT-D3+*U*-Pyrite surface
Micro-flotation
s-Triazine
Adsorption-dispersion energies
Electronic properties
XPS-FTIR analysis

ABSTRACT

In this study the green (environmentally friendly) novel di-sodium 2,6-dithio-4-butyl-amino-1,3,5-Triazine (SDTBAT) collector also known as s-triazine molecule was designed and synthesised for use in sulphide minerals separation. The SDTBAT adsorption was investigated on pyrite mineral surface using computational density functional theory with dispersion correction and *U*-parameter (DFT-D3+*U*) as well as experimental methods. The chemical adsorption behaviour of SDTBAT collector was compared with the sodium normal butyl xanthate (SNBX) and sodium normal butyl dithiocarbamate (SNBDTC). Computationally, it was observed that the SDTBAT adsorbed through the S and N atoms, while SNBX and SBDTC adsorbed through S atoms onto pyrite Fe atoms. The adsorption energies followed the decreasing adsorption strength as: SDTBAT > SNBX > SNBDTC, which suggested that the SDTBAT had strong exothermic adsorption than xanthate and DTC. The experimental micro-flotation tests showed fast floating and higher recoveries of pyrite when using the SDTBAT collector compared to xanthate and DTC. The XPS and FTIR analysis of pyrite-SDTBAT revealed that the SDTBAT adsorbed through S and N atoms on Fe atoms. This clearly demonstrated that the SDTBAT was a potential collector to replace the xanthate collector due to its high flotation power for separation of sulphide minerals.

1. Introduction

Design of collectors for sulphide minerals separations is still one of the major challenges in the field of mineral processing and requires fundamental understanding to attain a well performing collector that can recover minerals efficiently. One major challenge is to design and synthesise an environmentally friendly collector that can perform better than the well-known xanthate collectors, which have high collecting power but low selectivity [1]. In recent years, the search for new chemical reagents having strong affinity and better selectivity for certain metal ions has received attention [2]. However, this had its own challenges of running a large number of time-consuming and expensive tests. Molecular modelling has the ability to screen potential collector molecules using minimal time and resources prior to beginning full laboratory testing [3]. However, the flotation process is extremely complex, with many contributing factors that are not easily probed using computational methods. These factors have led to comparison of computational outputs against experimental outputs.

Previously a study on comparisons of xanthate, dithiocarbamate and thiophosphate on pyrite and galena has been conducted using computer modelling and microcalorimetry method [4]. Recently, the density functional theory (DFT) method adsorption energies has been compared with the experimental flotation recoveries using oxycarbonyl thiocarbamate for chalcopyrite and demonstrated good correlation between the two methods [5]. In addition a comparison of computational with microcalorimetry method on interaction of xanthate of increasing chain length on dry and hydrated pyrite surface has shown that the adsorption energies increase as the hydrocarbon chain increases, in particular for neutral xanthate [3]. Furthermore, the DFT and experimental flotation recoveries methods were used to investigate the separation of chalcopyrite and pyrite using O-isopropyl-N-ethyl thiocarbamate (IPETC), O-isopropyl-N-diethyl-thionocarbamate (IPDETC) and S-allyl-N-diethyl-dithiocarbamate (ADEDTC) and also described their adsorption mechanisms [6]. It is therefore clear that measuring computational outputs against experimental outputs is the best method to screen different reagents. Other collectors such as 2-mercaptobenzoxazole

* Corresponding authors.
E-mail addresses: peace.mkhonto@ul.ac.za (P.P. Mkhonto), zhxr1984@126.com (X. Zhang).

https://doi.org/10.1016/j.surfin.2023.102820
Received 6 December 2022; Received in revised form 24 February 2023; Accepted 14 March 2023
Available online 21 March 2023

Table 1
Pyrite minerals key element contents (wt %).

Element	Cu	Fe	S	Zn	Ca	Mg	Al
Pyrite	<0.05	46.15	51.77	0.12	0.06	<0.05	0.07

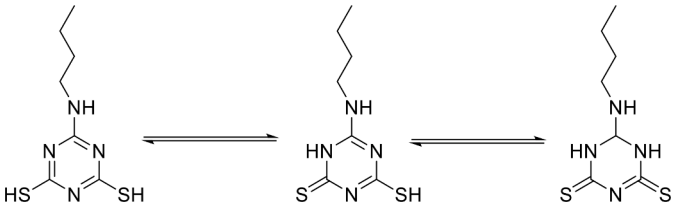

Fig. 1. . Possible tautomerization of the SDTBAT.

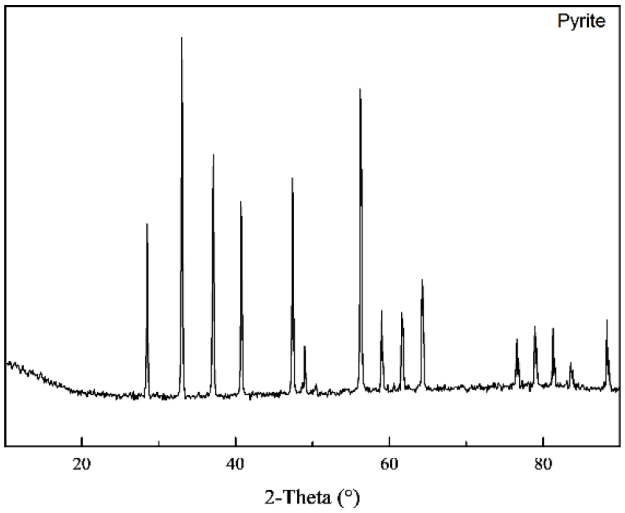

Fig. 2. The pyrite X-ray diffraction (XRD) patterns.

(MBO) for chalcocite (Cu_2S), 2-mercaptobenzothiazole (MBT) for galena (PbS) and 2-aminothiophenol (ATP) for sphalerite (ZnS) have been studied and have advantages since their selectivity is best at neutral pH [7]. It has been reported that the heterocyclic compounds can form hydrophobic complexes with many metals such as iron, copper, cobalt and nickel [8]. This suggested that the presence of a benzene ring or mercapto ring in collector reagents produces a highly selective collector.

The 1,3,5-triazine molecules, also called s-triazine compounds which are a class of nitrogen-containing heterocycles with a molecular formula of $C_3H_3N_3$ have not been given much attention and are potential collector molecules for sulphide minerals. The available literature that explored these type of molecules was on investigation of crosslinking of poly(vinyl chloride) fibers with 2-dibutylamino-4,6-dimercapto-1,3,5-triazine in the presence of sodium hydroxide and tetra-n-butylammonium bromide (TBAB) in water [9]. Investigation of sorption and adsorption of 2,4,6-tri(20-pyridyl)-s-triazine (TPTZ) complexes with iron(II) and ruthenium(III) on silica gel [10]. Another study used DFT+U to investigate the mechanical, structural, electronic and magnetic properties of s-triazine sheet (C_6N_6) with embedded Mn atom (Mn–C_6N_6) under the influence of external environment (symmetric deformation and perpendicular electric field) and found that the Mn–C_6N_6 system is structurally and mechanically stable and can serve as potential candidates for future spintronics and catalysis applications [11]. Furthermore, a DFT study was conducted on adsorption of CO_2, O_2, NO and CO on s-triazine-based g-C_3N_4 surface which demonstrated that the adsorption affinity of these gas molecules followed the order of $CO_2 > O_2 > NO > CO$ [12]. A theoretical study of di-amino-triazine (DAT, $C_{64}H_{68}N_{10}$), 1,4-bis(4-(2,4-diaminotriazine)phenyl)-2,3,5,6-tetrakis(4-tert-butyl phenyl) benzene adsorption on Cu(110) and Au(111) surfaces was also previously performed [13]. It is clear that the s-triazine compound have not been applied in mineral processing studies.

In the current research work, the computational density functional theory with dispersion correction and *U*-parameter (DFT-D3+*U*) was used to design the environmentally friendly di-sodium 2,6-dithio-4-butyl-amino-1,3,5-triazine (SDTBAT) collector for separation of sulphide minerals and investigated its adsorption on pyrite (100) surface. Thereafter the SDTBAT collector was synthesized and tested on pyrite minerals through experimental micro-flotation. The SDTBAT collector was compared to the performance of sodium normal butyl xanthate (SNBX) and sodium normal butyl dithiocarbamate (SNBDTC). The computed binding energies determined the affinity of the collectors with the mineral surface. The chemical reactivity of the collectors with pyrite surfaces was analysed from the spin-polarised local density of states and Bader analysis charges. These properties were accompanied by X-ray photoelectron spectroscopy (XPS) and Fourier-transform infrared spectroscopy (FTIR) analysis.

2. Materials and methodology

2.1. Computational methods

2.1.1. Density functional theory with dispersion correction

The density functional theory with dispersion correction and *U*-parameter (DFT-D3+*U*) study was carried out to investigate the pyrite bulk and (100) surface in interaction with SNBX, SNBDTC and SDTBAT. All calculations were performed using the Vienna *Ab-initio* Simulation Package (VASP) code [14,15]. The ion-electron interactions were represented by the projector augmented wave (PAW) method [16]. The electron-exchange correlations were represented by the generalized gradient approximation (GGA) with the Perdew-Wang functional (PW91) [17]. In all calculations the spin interpolation formula of Vosko et al. [18] was employed. All the calculations included the long-range dispersion correction approach by Grimme [19], with Becke-Jonson damping. The valence states were expanded in a plane-wave basis set with a cut-off at 450 eV for the kinetic energy, which was sufficient to converge the total energies during relaxations. The initial magnetic moments were described with low-spin distributions in Fe on both pyrite bulk and (100) surface. The Monkhorst-Pack grids of 8 × 8 × 8 k-points for bulk model and 3 × 3 × 1 k-points for (100) surface were employed, which ensured electronic and ionic convergence [20]. In order to improve the description of localized Fe d-orbitals states in the pyrite system, the Hubbard-*U* approximation was employed an approach used by Dudarev et al. [21]. Different values of the *U*-parameter (i.e. 1.5–1.8 eV) were varied on pyrite bulk Fe atoms based on previous reported

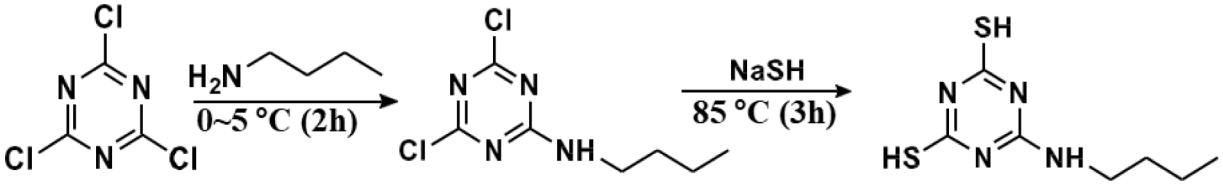

Scheme 1. Synthetic route for the 2,6-dithio-4-butylamino-1,3,5-triazine (SDTBAT) collector.

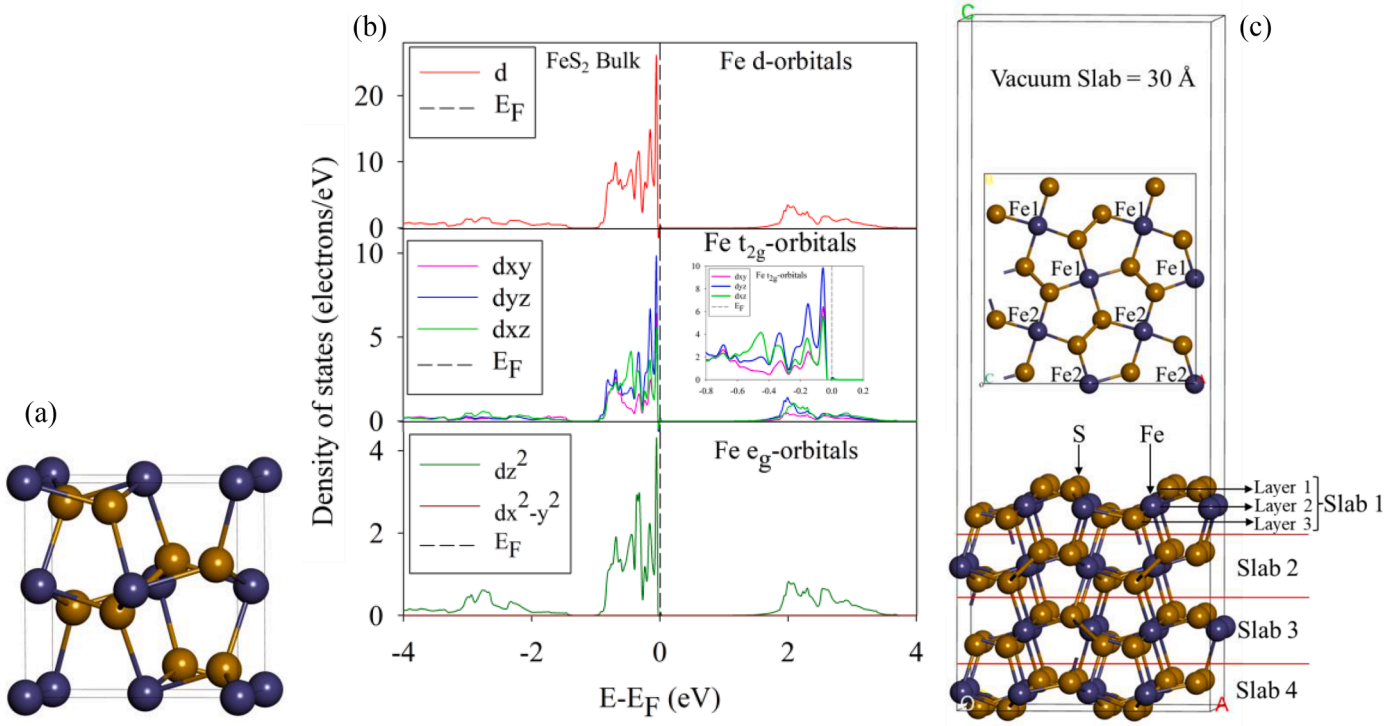

Fig. 3. Relaxed models and local density of states (LDOS): (a) FeS_2 bulk model, (b) FeS_2 bulk Fe PDOS and LDOS and (c) 2 × 2 (100) surface model.

Table 2
The surface coordination and surface energies for pyrite (100) surface.

Surfaces	Surface coordination		Surface energies
	Fe	S	$J.m^{-2}$
Bulk	6	4	N/A
(100) Surface	5	3	1.17

U-parameters (see Table S1) [22–24]. The resulting band gap and lattice parameters were compared to the experimental values. It was found that the $U = 1.7$ eV produced a band gap of 0.96 eV (0.95 eV) [24–26] as determined from band structures (see Fig. S1) and a lattice vector of a = 5.406 Å (5.417 Å) [27], which were in agreement with the experimental values in parenthesis. The geometry optimizations were obtained with the conjugate-gradient algorithm and considered converged when the force on each ion dropped below 0.02 eV.$Å^{-1}$, with the self-consistency of the electron density set to 10^{-6} eV. In order to improve the convergence of the Brillouin-zone integrations, the partial occupancies were determined using the Methfessel-Paxton smearing with a set width for all calculations of 0.2 eV. In order to obtain accurate electronic structures the tetrahedron method with Blöchl correction smearing, with a set width of 0.02 eV for bulk, surface and adsorbed surface calculations were employed.

Now, in order to calculate reaction energies, the optimization of SDTBAT, SNBX and SNBDTC models were performed in a cubic cell of 40 Å, which was enough to minimize spurious mirror-image interactions between collector molecules in adjacent supercells. The PAW pseudopotential, cut-off energy at gamma point and other precision parameters as in the surface calculations were employed. Note that the sodium ions (Na^+) were included in the simulation of the collector to neutralise the negatively charged sulphur (S^-) atom/s of the collector polar site. It has been reported that there was greater association of the Na^+ with S^- of collectors such as MBT^- [28]. Furthermore, it has been recently reported that neutral xanthate of increasing chain length adsorption on pyrite surface using computational method gave good correlation with microcalorimetry experiments compared to charged xanthates [3].

2.1.2. *Electronic properties and energy calculations*

The density of states for the isolated collectors were computed using Gaussian smearing with a set width of 0.03 eV, since tetrahedron method with Blöchl correction smearing could not be performed at gamma point. The charge states of the ions at the bulk, (100) surface and adsorbed (100) surface were discussed on the basis of a Bader analysis, an algorithm and a program developed for this purpose by Henkelman et al. [29,30]. In this case the tetrahedron method with Blöchl correction smearing was also employed. This algorithm consists of integrating the electron density in a region defined for each atom in such a way that the density gradient flux through the dividing surfaces is zero [31]. The charge density difference upon adsorption was determined by calculating the charge density for the adsorbed system (surface-collector) first and then for the unadsorbed pyrite (100) surface and finally for the collector molecules alone, each in the optimized geometry obtained for the adsorbed system. The difference between the charge density distribution of the adsorption system and the sum of the distribution for the (100) surface and the collector adsorbate are based on Eq. [1] [32]:

$$\rho(\text{Surface} + \text{Collector}) - \rho(\text{Surface}) - \rho(\text{Collector}) \quad (1)$$

which reveals the distribution of charge upon adsorption. The VESTA software [33] was used to visualize the charge density difference between the collector adsorbed surface system and the unadsorbed surface plus the collector molecule.

The relaxed surface energy was computed using Eq. [2] [34–36]:

$$E^R_{Surf.} = \frac{E^R_{Slab} - (n_{slab})E_{Bulk/atom}}{2A} \quad (2)$$

where the total energy of the surface is given by E_{slab}, the total energy of the bulk per total number of atoms in the bulk given by E_{bulk}/atom, the number of atoms of the surface is denoted by n_{slab} and the surface area is denoted as *A*.

The adsorption energies ($E_{ads.}$) of the collector molecules on the surface were calculated using Eq. [3]:

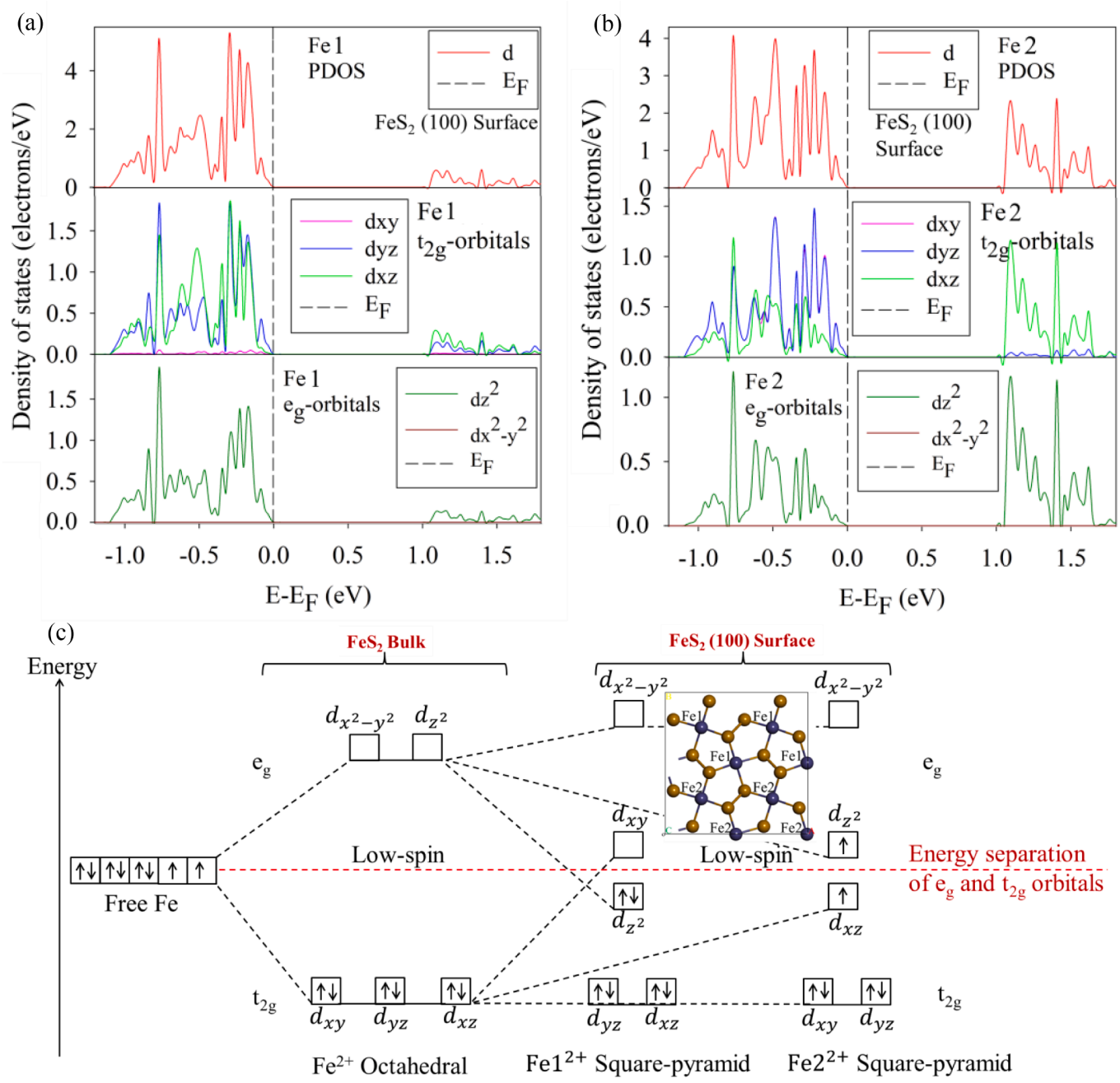

Fig. 4. The local density of states (LDOS) of pyrite (100) surface ((a) $Fe1^{2+}$ atoms, (b) $Fe2^{2+}$ atoms) and (c) Fe^{2+} atoms molecular orbitals of bulk and (100) surface.

Table 3
Calculated Bader analysis charges ($|e^-|$) for the pyrite bulk and (100) surface.

Atoms	Bulk	(100) Surface
Fe	+0.62	+0.66
S1	–0.32	–0.35
S2	–0.30	

$$E_{ads.} = E_{[S+C]} - \left(E_{[S]} + E_{[C]}\right) \quad (3)$$

where a negative value shows an exothermic favourable reaction between the collector molecule and the surface, whereas a positive value reveals the opposite. The contribution of dispersion energy in all the adsorption energy was calculated in a similar way.

Table 4
The selected polar sites bond lengths (Å) and angles (deg.°) on relaxed geometry of isolated SNBX, SNBDTC and SDTBAT collectors.

Bonds	SNBX	SDBDTC	SDTBAT
C4–S1	1.710	1.721	N/A
C4–S2	1.705	1.727	N/A
C2–S2	N/A	N/A	1.726
C6–S1	N/A	N/A	1.725
C4–O/N	1.352	1.349	1.376
S1–C4–S2	127.25	126.09	N/A

2.2. Experimental methods

2.2.1. Materials and reagents

Pyrite was purchased from Hubei Province in China and its purity

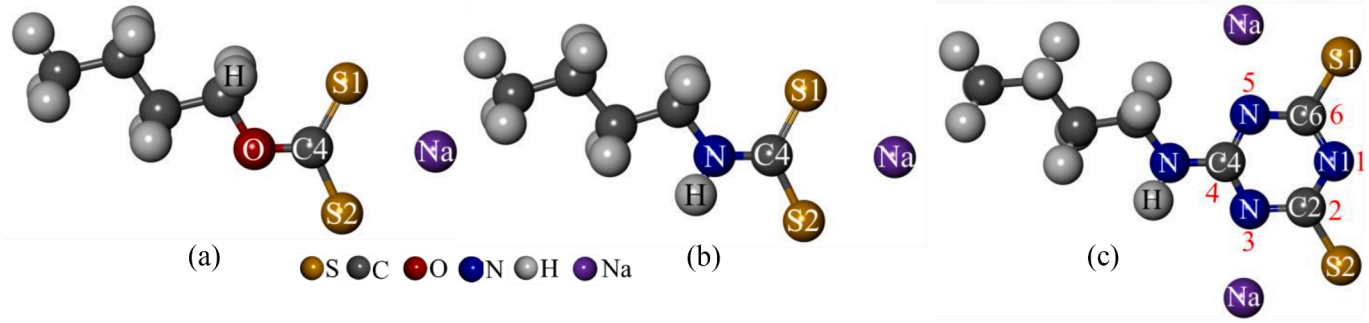

Fig. 5. The relaxed molecular geometries of the collectors: (a) SNBX, (b) SNBDTC and (c) SDTBAT.

Table 5
Calculated band gaps (eV) and Bader charges (|e⁻|) for the SNBX, SNBDTC and SDTBAT collectors.

Collector	Band gap	S1	S2	N1
SNBX	2.696	–0.32	–0.28	N/A
SDBDTC	2.703	–0.41	–0.44	N/A
SDTBAT	2.247	–0.36	–0.41	–1.02

was characterized from X-ray diffraction (XRD) to confirm the single phase samples. The pure minerals were handpicked then pulverised in a ceramic ball mill, there after crushed in a porcelain mortar and dry sieved to get particle sizes between 38 and 74 μm fractions prior to the micro-flotation. The purities of pyrite was found to be approximately 97.10% as calculated using the chemical assays of S as shown in Table 1 and the theoretical grade of S (53.33) according to Eq. (4) and also on the basis of XRD (Fig. 2). The pyrite samples were stored at approximately 5°C in a vacuum desiccator in a refrigerator.

$$\text{Mineral purity} = \frac{\text{Chemical assay}}{\text{Theoretical grade}} \times 100\% \quad (4)$$

The green (environmentally friendly) sodium 2,6-dithio-4-butylamino-1,3,5-triazine (SDTBAT) collector reagent was synthesized in BGRIMM Technology Group lab by adding equivalent of n-butylamine to the dispersion of 2,4,6-trichloro-1,3,5-triazine in crushed ice at 0~5°C with strong agitation for 1~2h; then 2 times of NaSH was added in batches at 25~30°C for 2h and at 85°C for 3h and then acidified the reaction mixture to precipitate the product, which yielded purity of

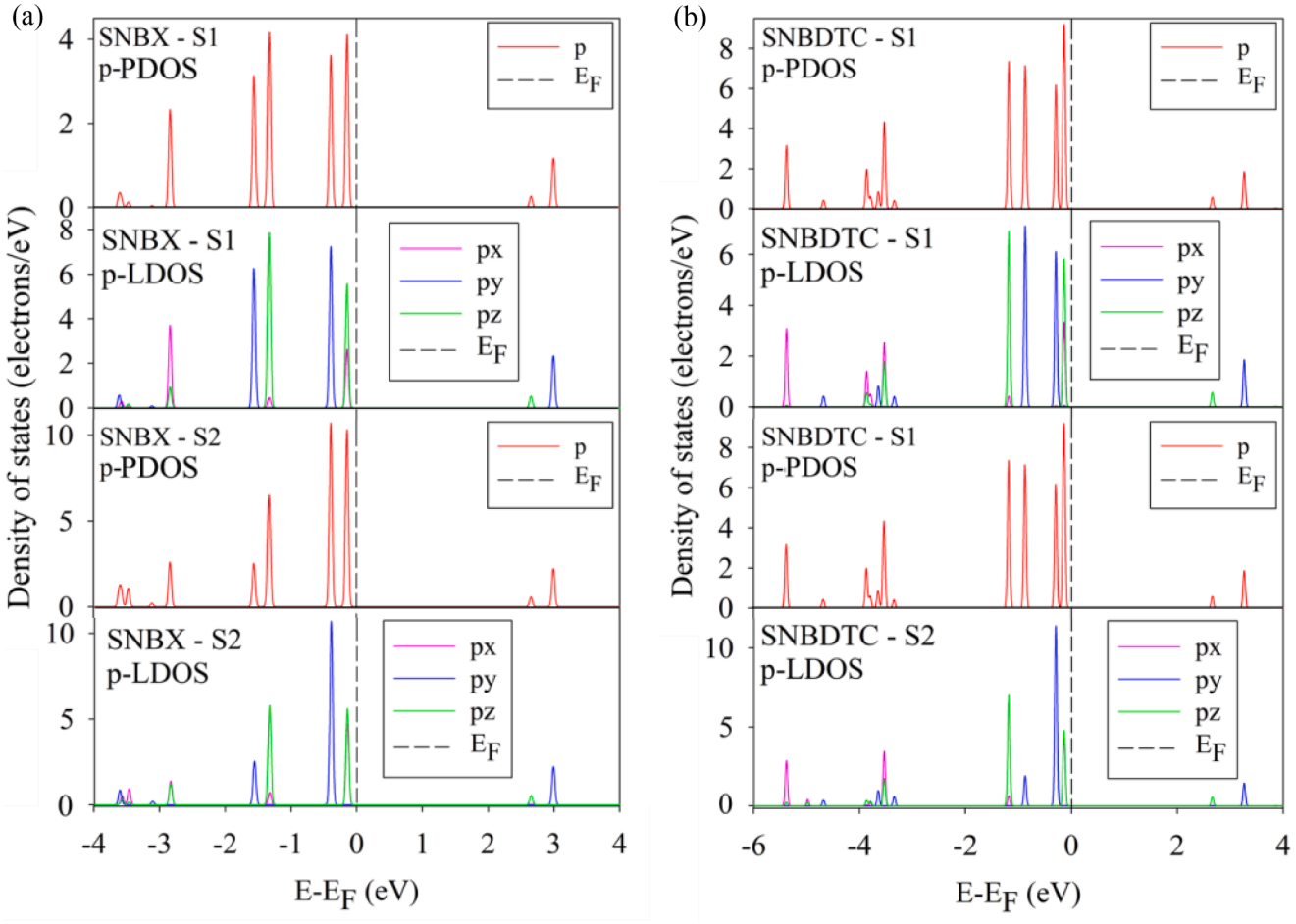

Fig. 6. The partial and local density of states: (a) SNBX and (b) SNBDTC collectors.

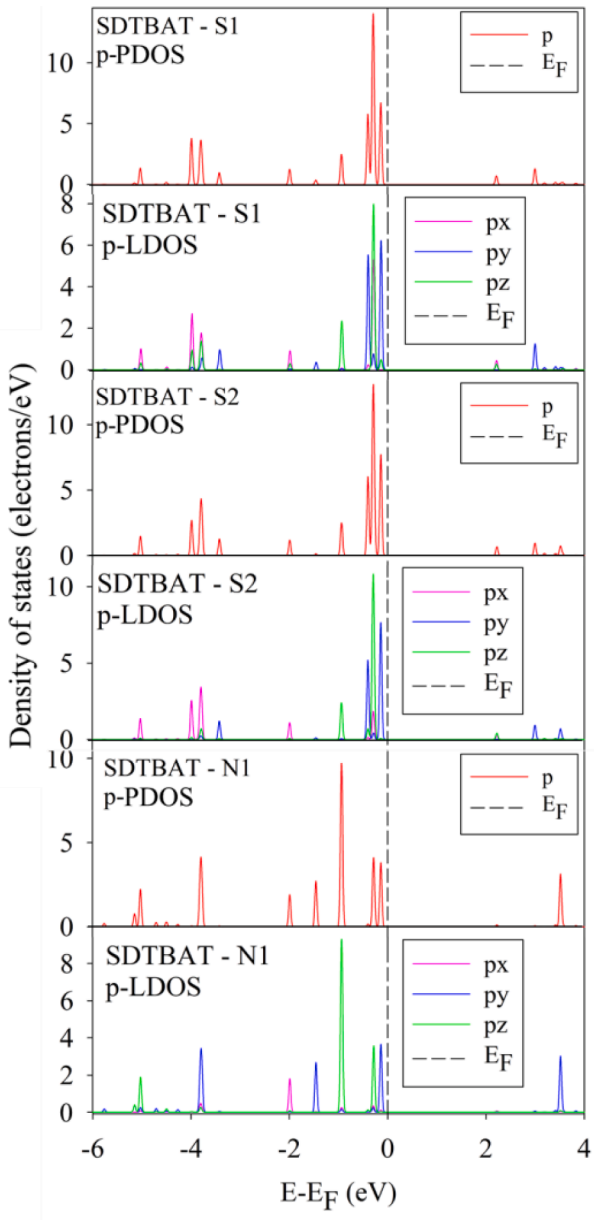

Fig. 7. The partial and local density of states of SDTBAT collector.

95.3% as illustrated in Scheme 1. Fig. 1 displays the possible tautomerization of the SDTBAT. The methyl isobutyl carbinol (MIBC) was purchased from Sinopharm Chemical Reagent Co., Ltd., China and was used as the frother. The distilled water was used in the experiments.

2.2.2. Micro-flotation

The flotation performance of the SNBX, SNBDTC and SDTBAT on pyrite mineral using micro-flotation experiments are described in this section. In this experiment the pH for flotation process was adjusted to approximately 9.0 with dilute NaOH solutions, and the frother (MIBC) dosage was 20 mg.L^{-1}. A 40 mL plexiglass cell was used on the XFG5-35 flotation machine for the micro-flotation tests of pyrite minerals. The agitation speed was set at 1752 r.min^{-1}. The flotation test began by addition of collector and then the MIBC frother to the slurry each after two minutes (2 min) of stirring. The mineral recoveries were collected for 4 min. The recovered concentrates were collected and dried in an oven and afterwards weighed and then the percent recoveries were computed from Eq. (5).

$$\text{Recovery } (\%) = \frac{\text{Mass of mineral in concentrate}}{\text{Mass of mineral in feed}} \times 100\% \quad (5)$$

Finally, the recovery of the froth products was used to assess the flotation performance of the collectors on pyrite minerals.

2.2.3. XPS analysis

Thermo Scientific K-Alpha+ instrument (Thermo Fisher, USA) with a mono Al-*Kα* excitation source (hν = 1486.6 eV) measurements for X-ray photoelectron spectroscopy (XPS) was used for surface chemical analysis on pyrite before and after SDTBAT treatment. Similar method was adopted in previous study [6]. A total of 2.0 g of pyrite and 30 mL of distilled water were added into a 100 mL conical flask with or without 2.0 mg.L^{-1} dosage of SDTBAT. The solution was stirred at room temperature (25°C) for 30 min in a thermostatic oscillator and thereafter the mineral samples were filtered, washed with distilled water, dried, and then loaded to XPS analysis. In the XPS measurements, the vacuum in the analytical chamber was 5 × 10^{-9} mbar. The XPS survey scans were conducted between 0 eV and 1200 eV with pass energy of 150.0 eV and a step size of 1.00 eV. The high-resolution XPS with pass energy of 50.0 eV and a step size of 0.10 eV was performed over five scans. The 284.8 eV of C 1s was used as the calibration binding energy (B.E.).

2.2.4. FTIR analysis

Fourier-transform infrared spectroscopy (FTIR) spectra was recorded by an iS10 FT-IR spectrometer in the range of 500–4000 cm^{-1} through KBr pellets at room temperature (25±1°C). The treated pyrite samples were prepared as follows: 1.0 g pyrite samples with particle size of less than 5 μm were placed into 30 mL SDTBAT solution with a concentration of 20.0 mg.L^{-1} at pH of around 9.0 and stirred for 30 min. Thereafter the

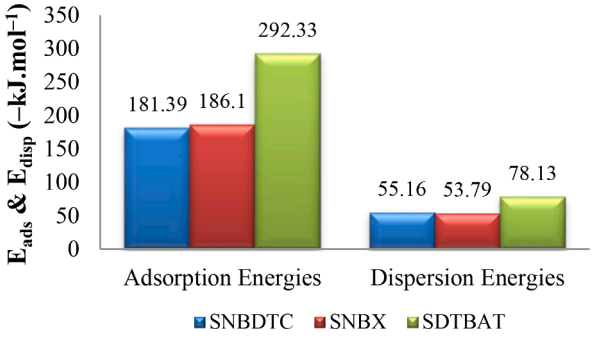

Fig. 8. Bar graph displaying the most exothermic adsorption and dispersion energies trends for SNBX, SNBDTC and SDTBAT collectors adsorption on pyrite (100) surface.

Table 6
The adsorption and dispersion energies (kJ.mol^{-1}), and bond lengths (Å) of SNBX, SNBDTC and SDTBAT adsorption on pyrite (100) surface.

Molecule	$E_{ads.}$	$E_{disp.}$	Chain	Head adsorption	Fe1–S1	Fe2–S2	Fe3–N1
SNBX	–167.89	–40.75	vertical	bidentate binuclear	2.305	2.290	N/A
SNBX	–186.10	–53.79	flat	bidentate binuclear	2.297	2.285	N/A
SNBDTC	–163.07	–41.98	vertical	bidentate binuclear	2.309	2.297	N/A
SNBDTC	–181.39	–55.16	flat	bidentate binuclear	2.329	2.282	N/A
SDTBAT	–269.13	–63.64	vertical	tridentate trinuclear	2.320	2.257	2.140
SDTBAT	–292.33	–78.13	flat	tridentate trinuclear	2.324	2.327	2.108

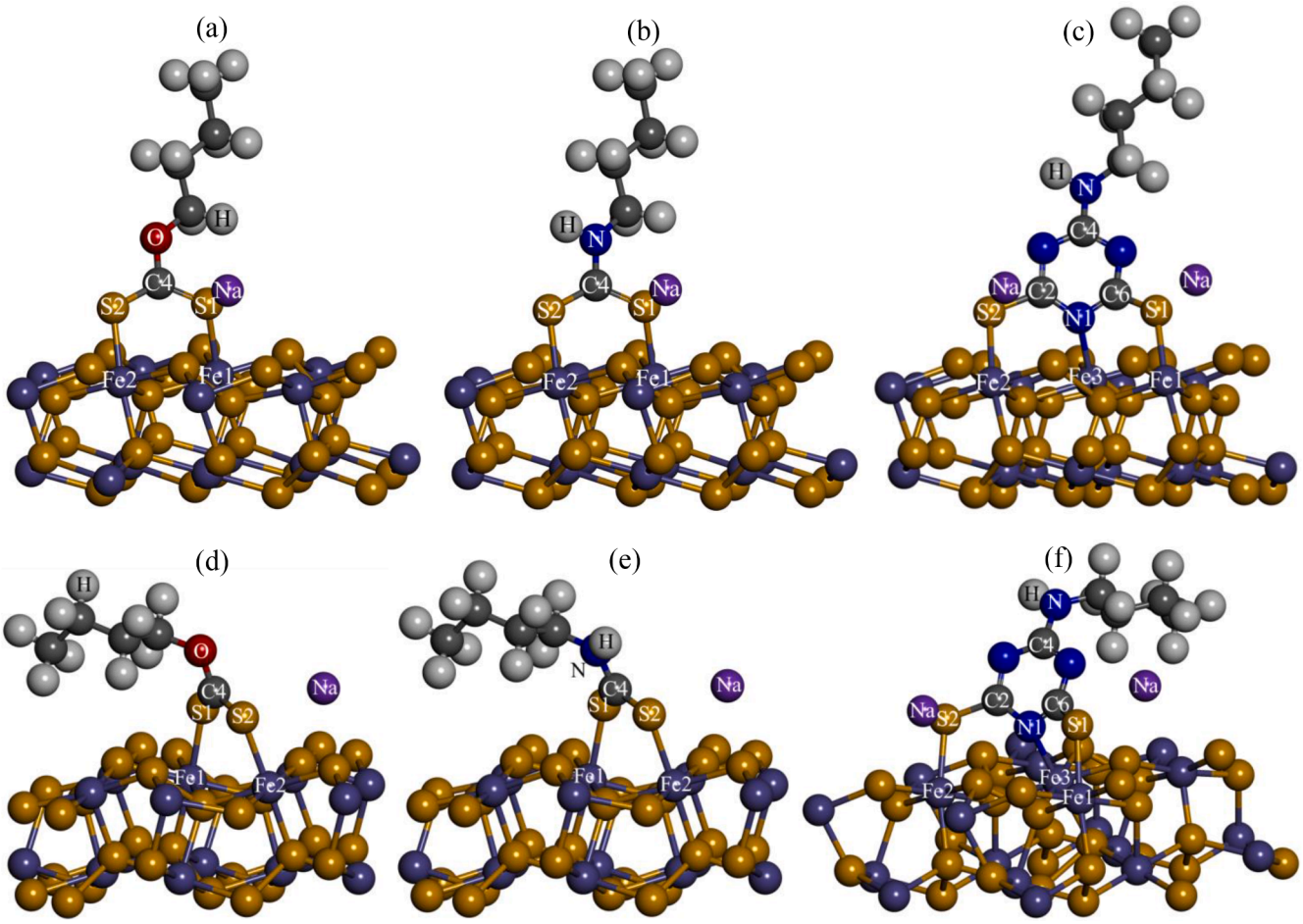

Fig. 9. Relaxed geometries of collectors' adsorption on pyrite (100) surface: (a) SNBX (vertical), (b) SNBDTC (vertical) and (c) SDTBAT (vertical), (d) SNBX (flat), (e) SNBDTC (flat) and (f) SDTBAT (flat) adsorptions.

treated pyrite samples were filtrated and dried under vacuum for 24h. Finally, the SDTBAT collector, the treated and untreated pyrite samples were used to measure their FTIR spectra.

3. Results and discussion

3.1. Pyrite bulk and (100) surface models and electronic properties

The relaxed bulk model of pyrite (FeS_2) with space group symmetry of Pa-3 (Fig. 3a) was used to cleave the 2 × 2 (100) surface (Fig. 3b). Pyrite was defined as a low-spin, where the Fe^{2+} d-orbital splitting were occupied in the order of t_{2g}^6 and e_g^0, as adopted in this study. The surface terminations without dipole were adopted in the study. The 2 × 2 (100) surface model was composed of 12 atomic layers and the periodic cells of 10.811 × 10.811 × 39.352 Å was used and possessed a vacuum slab separation of 30 Å in order to avoid interaction between the collectors and the mirror image surface. In the adsorption system the bottom six layers (6L) were kept fixed to bulk coordinate, while the top six layers (6L) were relaxed and allowed to interact with the collectors. Table 2 shows the calculated surface energy for pyrite (100) surface which illustrated the effect of the DFT-D3+*U*.

The computed local density of states (LDOS) of the pyrite bulk and (100) surface are shown in Fig. 3b, where a clear contribution of the t_{2g} (dxy, dyz, dxz) and e_g (dz^2, dz^2-y^2) to the d-orbitals partial density of states (PDOS) is displayed. For the bulk model it is clear that the t_{2g} orbitals are fully occupied, while the e_g orbitals have the dz^2 orbital partially occupied, while the dx^2-y^2 orbital is empty. It was noted that the dyz have higher states compared to the dxy and dxz orbitals, which demonstrated that the partial occupation of the dz^2 was largely from dxy and dxz orbitals as shown in Fig. 3b. This suggested that there was some intrinsic mixing of the dz^2 with dxy and dxz orbitals, and clearly the dz^2 and dx^2-y^2 were non-degenerate with the dx^2-y^2 higher in energy and did not hybridise with any orbitals (see Fig. 3b). At the (100) surface, the Fe atoms d-orbitals degeneracies within the t_{2g} and e_g states clearly were lost as a consequence of the lower bonding symmetry from distorted octahedral coordination to 5-coordination roughly square-pyramidal [37]. Previously, it was reported that the square-pyramid was composed of dx^2-y^2 and dz^2 as the σ orbitals in the e_g, and dxy, dxz and dyz as the π orbitals in the t_{2g} [6]. These were also previously outlined by Chen [38]. The σ orbital are unoccupied orbitals, while the π orbitals are electron pairs. These were discussed based on theory and partial density of states. However, the current results based on LDOS clearly depict a different behaviour from our previous report [6].

The LDOS as displayed in Fig. 4a and b, clearly showed that the (100) surface possessed two different Fe atoms namely Fe1 and Fe2. The dz^2 orbital of Fe1 atoms lowered in energy and overlapped into the t_{2g} orbitals and was fully occupied, while the dxy orbital had almost zero states and therefore empty (see Fig. 4a). The Fe2 atoms had the mixing of the dz^2 and dxz orbitals and were equally occupied, which suggested that they shared the two electrons as shown in Fig. 4b. These were also demonstrated by the molecular orbital in Fig. 4c. Moreover, the anti-bonding orbitals (LUMO) of the Fe2 atoms were largely from the dxz and dz^2 orbitals. The Fe2 atoms dxy and dyz were fully and equally occupied. On both Fe atoms (Fe1 and Fe2) the dx^2-y^2 orbitals were empty and did not form any hybridisation. This suggested that there is a shift of Fe dz^2 states to higher energy and a slight destabilization of dxz and dyz states

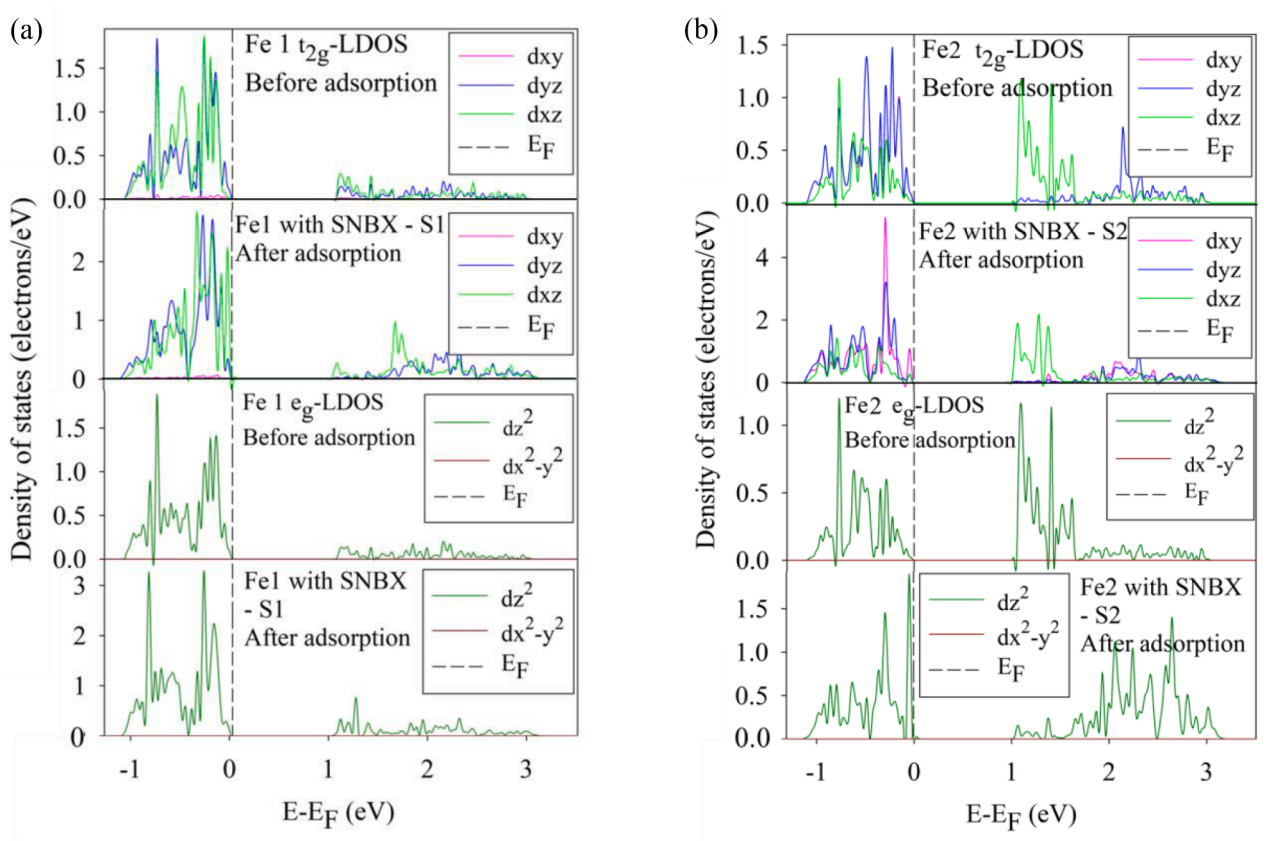

Fig. 10. The local density of state (LDOS) of pyrite (100) surface adsorbed with SNBX collector: (a) Fe1 t_{2g} and e_g LDOS and (b) Fe2 t_{2g} and e_g LDOS, before and after adsorption.

relative to dxy. Significantly, the location of the dxy at higher energy than dxz and dyz was previously reported [39]. Furthermore, Based on the behaviour of the Fe1 and Fe2 atoms d-orbitals it was suggested that the low spin property of bulk pyrite (Fe d^6) could be converted to high-spin (unpaired) at the (100) surface as seen on Fe2, while Fe1 maintains the low-spin (paired), and such was previously proposed by Bronold et al. [39]. These observations suggested that in the surface adsorption, for Fe1 atoms, the dyz and dz^2 will be the most probable HOMO orbitals, while for Fe2 atoms the dxy and dyz will be the HOMO orbital. The LDOS have demonstrated that the dyz were the most active orbitals and will participate significantly in the hybridisation reactivity of the surface with collectors' p-orbitals. These insights have unravelled the contribution of the t_{2g} and e_g orbitals to the summed d-orbitals PDOS. The TDOS of the bulk and LDOS of the S atoms both on bulk and (100) surface are shown in the supporting information Fig. S2.

The computed Bader charges of the bulk and (100) surface are shown in Table 3. Although the Fe atoms displayed different LDOS behaviour on the surface, their Bader charges are the same. However, the S atoms on the bulk gave two different Bader charges, which were attributed to the effect of the Fe atoms. On the (100) surface it was found that the S atoms possess the same Bader charges.

3.2. Isolated xanthate, dithiocarbamate and s-triazine molecular geometries and electronic properties

The SNBX, SNBDTC and SDTBAT models were relaxed in isolation and their relaxed bond lengths are shown in Table 4. The main focus was on the centre of reactivity C–S group atoms of the collectors. As shown in Fig. 5, the C4–S1 possessed a double bond and the C4–S2 possessed a single bond on SNBX and SNBDTC. In addition the C–S bonds of SDTBAT were single bonded. The negative charge on the S atoms forming single bonds was neutralised by the sodium (Na^+) cation. Table 4 shows that the C4–S1 and C4–S2 bond lengths on SNBX were shorter thus more stable than those in SNBDTC. The C4–S2 bond was shorter than the C4–S1 bond on SNBX, while on SNBDTC the C4–S2 bond was longer than the C4–S1 bond. The C6–S1 and C2–S2 bond lengths on SDTBAT were almost equal and similar to those of SNBDTC. In particular the SDTBAT C–S bond lengths were almost equal to that of C4–S2 single bond for SNBDTC, which showed the effect of nitrogen atoms in the C–S bonds. This suggested that SDTBAT will be more reactive than SNBDTC due to the s-triazine group. The N atoms will be responsible for the strong reactivity of SDTBAT, since the N atoms donates electron density towards the C atom and therefore induce strong reactivity of the S atoms with mineral surface as previously reported [6].

Table 5 depicts the reactivity of the xanthate, dithiocarbamate and s-triazine collectors from the Bader charges. The adsorption strength of thiol collectors was based on the electron density on the centre-of-reactivity atom (i.e. S and N atoms), such that the atom with more negative charges will have the strongest adsorption (more exothermic). The atomic charges on the S1 and S2 atoms, as shown in Table 5, indicated more negative charge on SNBDTC, amongst the collectors. However, the SDTBAT N1 atoms possessed greater negative charges and therefore the N1 will have more influence in strong reactivity of the SDTBAT. As such the electronegativity decreased in the order: SDTBAT > SNBDTC > SNBX. This indicated that the SDTBAT had the highest probability to bind stronger on the surface and thus may have better flotation performance.

The total density of states (TDOS) shown in Fig. S3, together with the partial density of states (PDOS) and local density of states (LDOS) in Figs. 6 and 7 displays a direct band gaps for the collectors shifted towards the conduction band (CB). A molecule with the lowest band gap or small gap between HOMO and LUMO (H-L) was previously defined as more reactive than a molecule with a large gap [40]. The band gaps were determined from the TDOS (see Fig. S3) of the collectors as also

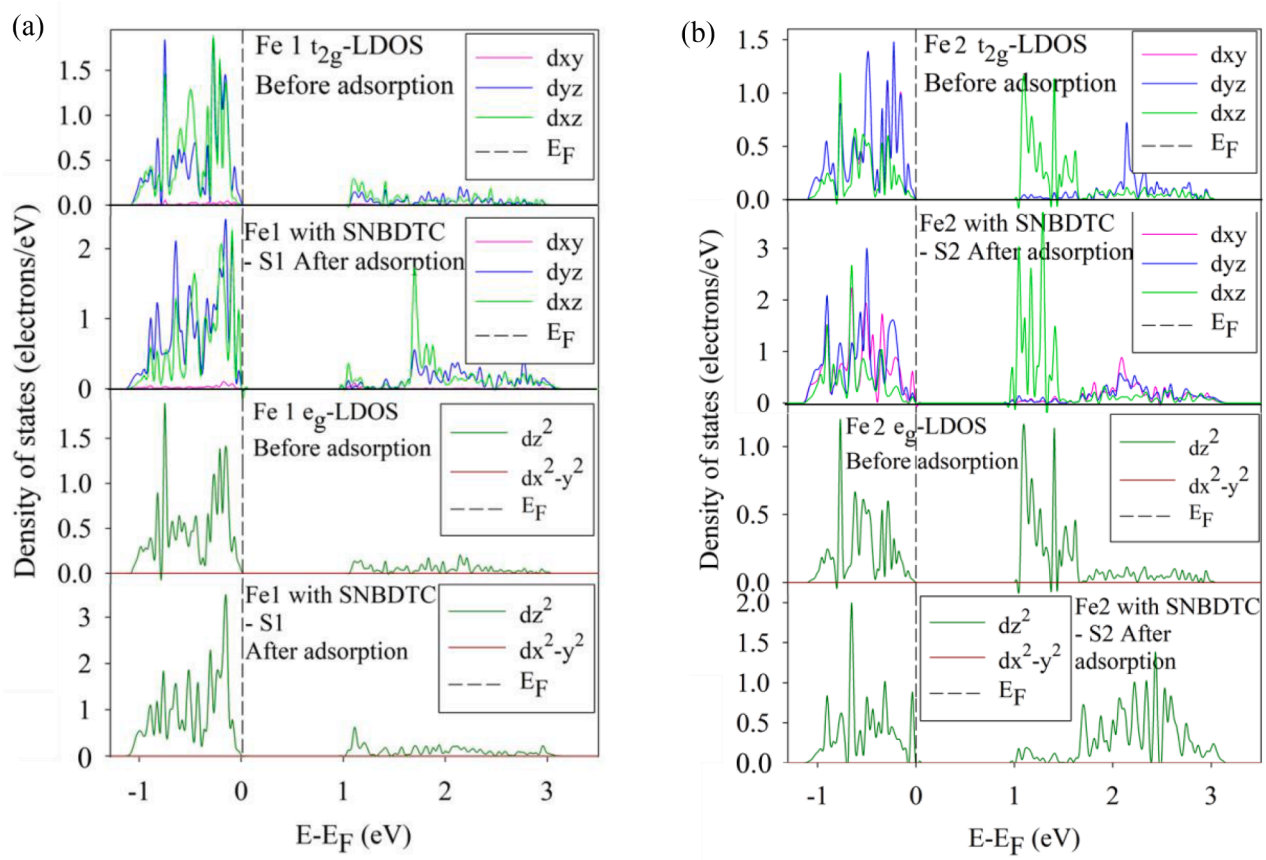

Fig. 11. The local density of state (LDOS) of pyrite (100) surface adsorbed with SNBDTC collector: (a) Fe1 t_{2g} and e_g LDOS and (b) Fe2 t_{2g} and e_g LDOS, before and after adsorption.

displayed in Table 5, which were found as 2.969 eV, 2.703 eV and 2.247 eV for SNBX, SNBDTC and SDTBAT, respectively. These results suggested that SDTBAT would be more reactive than SNBX and SNBDTC and the reactivity decreased in the order: SDTBAT > SNBX > SNBDTC.

In Figs. 6 and 7, the PDOS and LDOS of the SNBX, SNBDTC and SDTBAT S1, S2 and N1 atoms were examined and it was clear that they dominated the Fermi energy (E_F) with the highest states. These examinations depicted the contribution of the px, py and pz orbitals to the p-orbitals of the collectors. From the analysis of the LDOS it was clear that the pz and px were at the same energy just below the E_F, with pz higher in states than px on S1 and S2 atoms of SNBX and SNBDTC collectors (see Fig. 6), of which constituted the HOMO orbitals. The second occupied molecular orbital (SOMO) was clearly the py orbitals. However, on S1, S2 and N1 atoms of SDTBAT (Fig. 7), the py was the HOMO orbitals, while the px and pz, were the SOMO orbitals, with pz higher in states than px orbitals. These findings suggested that the collectors may offer their S atoms HOMO electrons to Fe atoms having $(t_{2g})^6(e_g)^\circ$Fe(II) configurations to form normal covalent bonds or back-donation covalent bonds on the surface of sulphide minerals [41].

3.3. Collector adsorptions on pyrite (100) surface

The adsorption of the collectors on pyrite (100) surface was initiated by positioning the collectors S atoms at approximately 2.00 Å on the Fe atoms, which has been found as the preferred stable adsorption site [3]. Two distinct adsorption modes were performed: 1) vertical and 2) flat adsorptions. The adsorption energies and dispersion energies are displayed in Table 6 and the most stable exothermic energies depicted in Fig. 8. The relaxed adsorption structures are shown in Fig. 9, where it was observed that the collector preferentially chemisorbed on the Fe atoms and formed stable six-membered Fe complexes. For all collectors i.e. SNBX, SNBDTC and SDTBAT collector adsorptions, the most favoured adsorption mode was the flat mode bonding in bidentate binuclear for SNBX and SNBDTC (Fig. 9d and e) and tridentate trinuclear for SDTBAT (Fig. 9f). The calculated energies for the most stable exothermic adsorptions were $E_{ads} = -186.10$ kJ.mol^{-1}, including $E_{disp} = -53.79$ kJ.mol^{-1} for SNBX, and $E_{ads} = -181.39$ kJ.mol^{-1}, including $E_{disp} = -55.16$ kJ.mol^{-1} for SNBDTC. The flat adsorption of SNBX produced the collector S atoms and surface Fe atoms bonds of Fe1−S1 = 2.297 Å and Fe2−S2 = 2.285 Å, while the SNBDTC established Fe1−S1 = 2.329 Å and Fe2−S2 = 2.282 Å bonds (Table 6). The SNBX was less exothermic with shorter Fe−S bond length than the previously reported PNBX on pyrite surface [3]. The Fe−S bond lengths of SNBX flat adsorption on average were shorter than those of SNBDTC flat adsorption, which indicated strong bonding of SNBX as depicted from the adsorption energies.

Furthermore, there was very little difference in the adsorption energies of SNBX and SNBDTC which indicated that the bonding was mainly though the S atoms and Fe atoms. This suggested that the presence of water would be crucial to detect a clear adsorption capacity difference between the two collectors. The S1–C4–S2 bond angle for flat SNBX and SNBDTC adsorptions were found to increase to 132.62° and 130.90° after adsorption, respectively. The vertical adsorptions of SNBX and SNBDTC also resulted in bidentate binuclear bonding (Fig. 9a and b). As expected the dispersion energies for the flat adsorption were more exothermic than the vertical adsorption (see Table 6). In addition the dispersion energies of SNBDTC were more exothermic than for SNBX in both vertical and flat adsorption. This clearly indicated that there was a strong interaction between the hydrocarbon chain and the surface resulting in strong long-range dispersion energies. Furthermore, the strong dispersion energies of SNBDTC compared to SNBX was ascribed to the N−H atoms having strong interaction with the surface compared

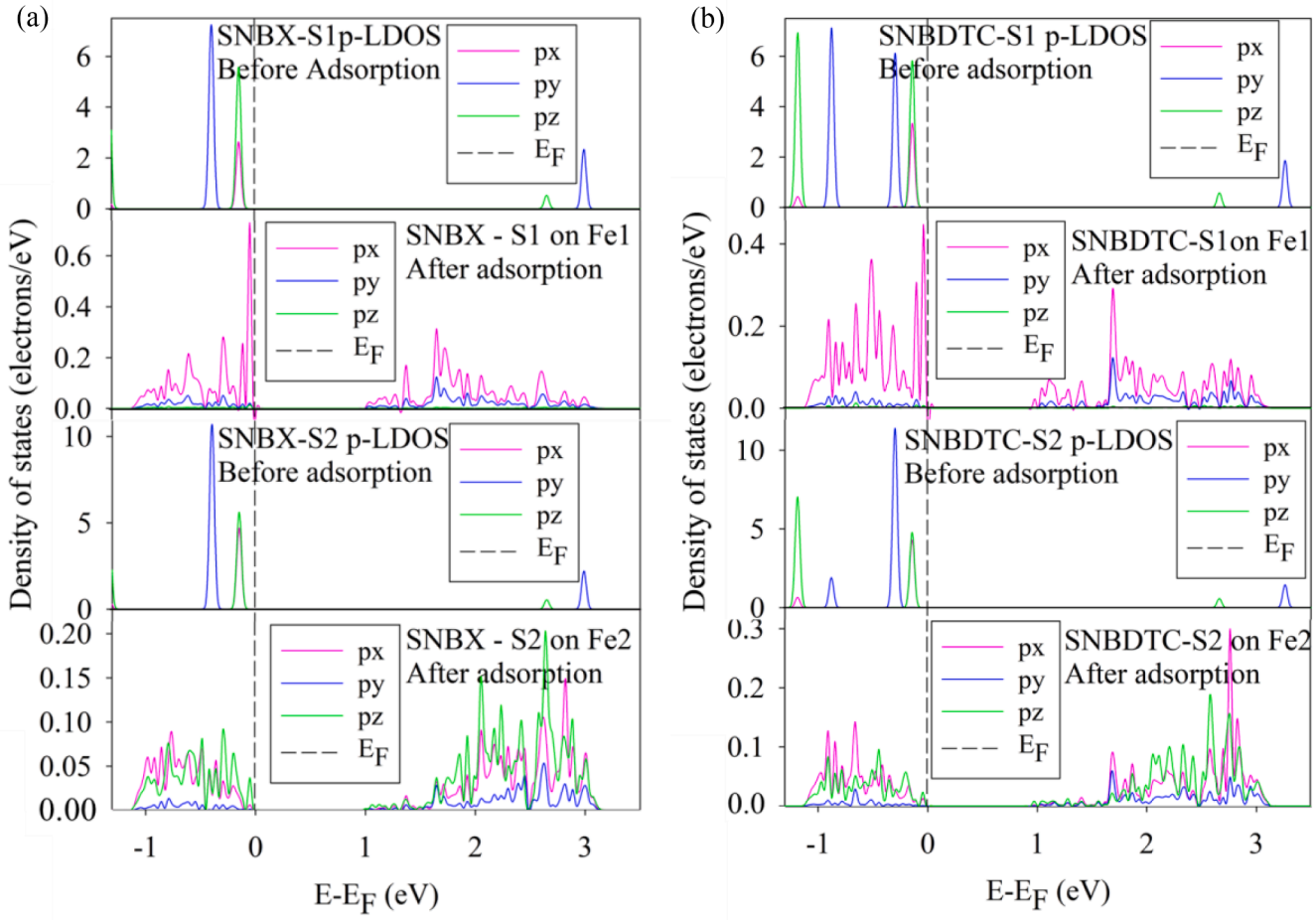

Fig. 12. The local density of state (LDOS) of S atoms of SNBX and SNBDTC collectors adsorbed on pyrite (100) surface: (a) SNBX S1 and S2 p-LDOS and (b) SNBDTC S1 and S2 p-LDOS, before and after adsorption.

to the oxygen atom on SNBX.

The tridentate trinuclear bonding of SDTBAT flat adsorption mode through S and N atoms on the surface (Fig. 9c and f), resulted in most stable exothermic $E_{ads} = -292.33$ kJ.mol^{-1}, including $E_{disp} = -78.13$ kJ.mol^{-1} (Table 6). It is clear that the adsorption and dispersion energies of flat adsorption were more exothermic than for vertical adsorption. This demonstrated the effect of dispersion interaction of the hydrocarbon chain with the surface. Furthermore, the adsorption and dispersion energies of SDTBAT were more exothermic than for SNBX and SNBDTC with pyrite surface (see Fig. 8). The vertical adsorption of S and N atoms of SDTBAT on surface Fe atoms produced bonds of Fe1−S1 = 2.320 Å, Fe2−S2 = 2.257 Å and Fe3−N1 = 2.140 Å, while flat adsorption formed Fe1−S1 = 2.324 Å, Fe2−S2 = 2.327 Å and Fe3−N1 = 2.108 Å bonds (Table 6). Although the vertical SDTBAT adsorption had strong Fe−S bond lengths than the flat adsorption, the Fe3−N1 bond was stronger for the flat adsorption than vertical adsorption. This showed that the N1 atom and the dispersion interaction had strong effect in strong adsorption of SDTBAT in a flat mode than vertical mode. The shorter Fe3–N1 bond length than the Fe−S bonds may be ascribed to the electronegativity of the N1 atom, thereby donating more electrons than the S atoms. This bonding behaviour clearly demonstrated the strong binding of the SDTBAT collector on pyrite (100) surface. In addition the s-triazine group also had strong dispersion interaction with the surface. This clearly revealed that the s-triazine collector (SDTBAT) was a better collector than the xanthate and dithiocarbamate collectors. This suggested that SDTBAT may be highly powerful in the flotation of pyrite and its flotation performance will be discussed in the micro-flotation section.

3.4. Electronic properties of collectors adsorption on pyrite (100) surface

The LDOS for the adsorption of the SNBX, SNBDTC and SDTBAT collectors on the pyrite (100) surface were computed to gain more insight into their electronic behaviour. Figs. 10 and 11 shows the LDOS of pyrite Fe atoms before and after adsorption. The description of surface and molecules chemistry of interaction has always been described from summed PDOS, which are constituted by the LDOS. Therefore in the current study the description was analysed in depth from the LDOS for both surface Fe and collector S atoms. For Fe1 atom, as shown in Fig. 10a, the t_{2g} orbitals e_g orbitals hybridised with the p-orbitals of the SNBX S1 atom. It was observed that the dxy did not change and was almost at zero states, while the dyz, dxz and dz^2 increased in states, with the dxz dominating just below the E_F with higher states than the dyz. Significantly the dyz and dz^2 displayed the highest states sharp peaks shifted towards the E_F, with the dz^2 peak higher in states. This behaviour demonstrated that the dxz was the most active orbital. Furthermore, there was electron gain largely in the dxz and dz^2 orbitals. In Fig. 10b it is shown that the Fe2 LDOS t_{2g} and e_g orbitals mixed with SNBX S2 atom p-orbitals. In this case the dxy and dz^2 clearly increased in states largely and were shifted towards the E_F. The dxy displayed the highest states sharp peak, while the dz^2 displayed the highest states sharp peak just below the E_F and therefore illustrated that they have strong hybridisation with the S2 of SNBX collector. It was noted that the dz^2 LUMO splitting peaks were shifted to higher energy.

The Fe1 atom t_{2g} and e_g orbitals hybridisations with the p-orbitals of the SNBDTC S1 atom are shown in Fig. 11a. For this adsorption the dxy did not change and still at almost zero states, while the dyz, dxz and dz^2

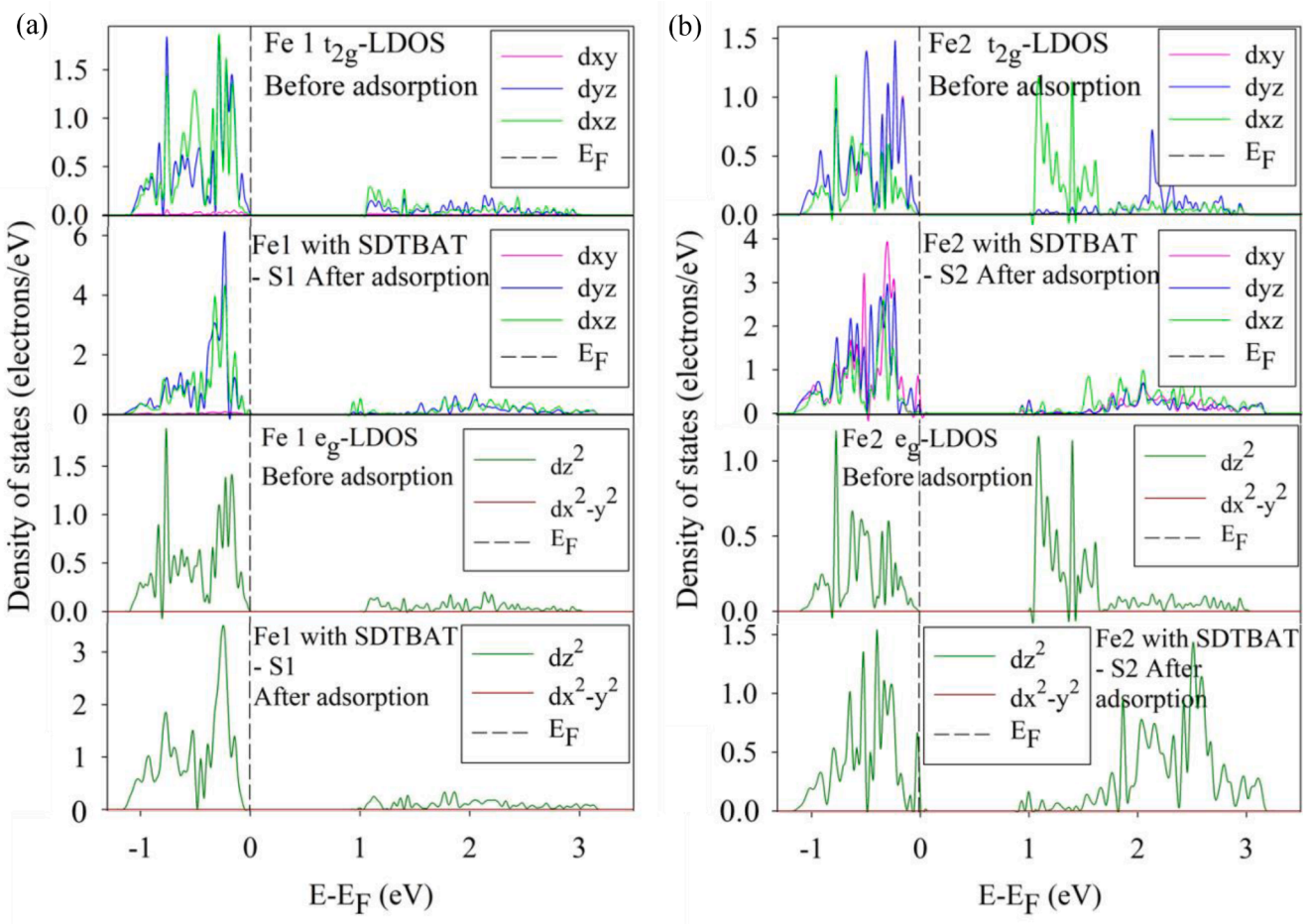

Fig. 13. The local density of state (LDOS) of pyrite (100) surface adsorbed with SDTBAT collector: (a) Fe1 t_{2g} and e_g LDOS and (b) Fe2 t_{2g} and e_g LDOS, before and after adsorption.

increased in states, with the dxz dominating just below the E_F.This demonstrated that there were electron gains in the dyz, dxz and dz^2 orbitals. As shown in Fig. 11b the t_{2g} and e_g orbitals for Fe2 atom interacted with SNBDTC S2 atom p-orbitals. It was clearly noted that also in this interaction the dxy and dz^2 dominated just below the E_F. This illustrated that there was greater electron gain in the dxy and dz^2 which were the most active orbitals and strongly hybridised with the p-orbitals of S2 atom of SNBDTC collector. A sharp LUMO peak of dxz was noted which increased in states at around 1.5 eV. The dz^2 LUMO splitting peaks were shifted to higher energy.

The SNBX S atoms p-LDOS as shown in Fig. 12a display electron loss, due to reduced states. For SNBX S1 atoms the py and pz orbitals largely reduced states to almost zero, while the px displayed a sharp peak just below the E_F. Moreover, the pz reduced to zero states at the valence band (VB). Based on the behaviour established on the Fe1 atoms where electrons gains were largely on the dyz, dxz and dz^2 orbitals, this emanated from a strong mixing of the dyz, dxz and dz^2 orbitals with SNBX S1 atoms, py and pz orbitals. This was because the orbitals are pointing in the same y and z directions. The SNBX S2 atom in Fig. 12a clearly showed that the py was largely reduced in states compared to px and pz, with py at almost zero states at the VB. This also indicated electron loss towards the Fe2 atom. Also in this case, as it was observed that the Fe2 atoms accepted electrons into the dxy and dz^2, the SNBX S2 atoms clearly lost electrons from the px and py largely, which were deposited into the dxy, while those from pz were deposited into the dz^2 orbitals. This was also ascribed to the orbitals directions.

The SNBDTC S atoms p-LDOS as shown in Fig. 12b clearly indicated that there was electron loss, due to reduced states. For SNBDTC S1 atoms, the py and pz orbitals have largely reduced states compared to px, with the pz at zero states indicating greater electron loss. From the analysis of the Fe1 atoms LDOS, it was clear that there was a strong mixing of the dyz, dxz and dz^2 orbitals with px, py and pz orbitals of the SNBDTC S1 atom. This occurred due to orbitals pointing in the same y and z directions. And therefore, the px and py have transferred electrons into the dxz and dyz orbitals, while the pz transferred into the dz^2 orbitals, respectively. The SNBDTC S2 atom in Fig. 12b clearly showed that the py was largely reduced in states compared to px and pz, with py at almost zero states in the VB. This also indicated electron transfer towards the Fe2 atom.

The surface Fe atoms t_{2g} orbitals e_g orbitals hybridisations with the p-orbitals of the SDTBAT S atoms are shown in Figs. 13 and 14a. Note that Fe1 and Fe3 atoms had the same LDOS behaviour before adsorption on the surface. In the adsorptions, the Fe1 interacted with S1 (Fig. 13a), while Fe3 interacted with N1 (Fig. 14a) and therefore the behaviour would change. For both Fe1 and Fe3 atoms the dxy did not change and was still at almost zero states, while the dyz, dxz and dz^2 increased in states. Also for Fe1 atoms the dyz was higher in states than the dxz, while on Fe3 the dxz was higher in states than the dyz, both with a sharp peak at around –0.4 eV. This suggested that a large electron gain in the dyz and dz^2 for Fe1 was eminent, while Fe3 atom largely lost electrons from the dyz and dz^2 orbitals. In Fig. 13b, the t_{2g} and e_g orbitals for Fe2 atom adsorbed with SDTBAT S2 atoms showed that the dxy and dz^2 dominated just below the E_F. Furthermore, the dxy was higher in states which illustrated greater electron gain in the dxy from the S2 atom of SDTBAT collector. In this adsorption the Fe2 atom LUMO (dxz and dz^2) splitting peaks in the conduction band (CB) were shifted to higher energy.

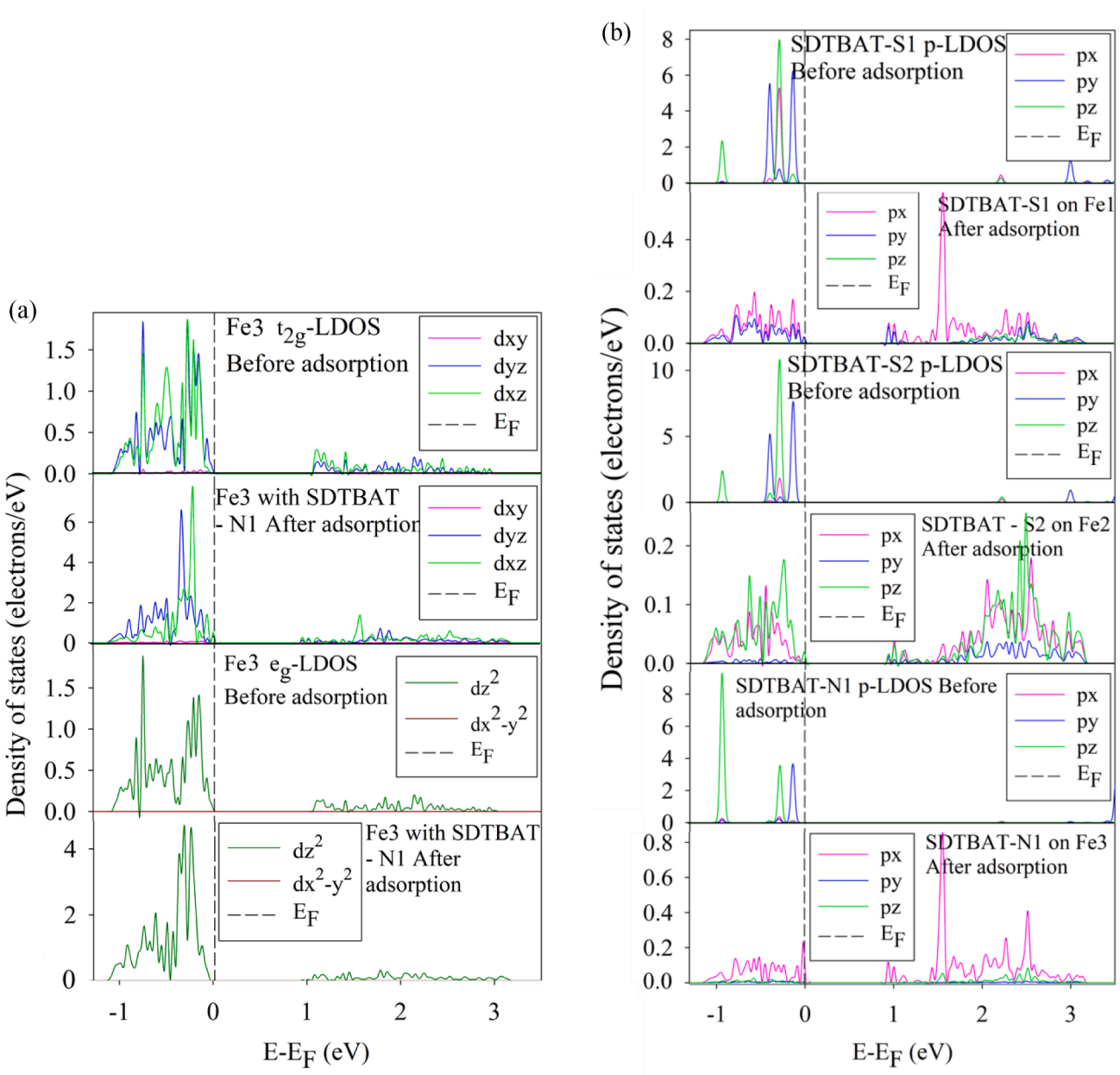

Fig. 14. The local density of state (LDOS) of pyrite (100) surface and SDTBAT collector: (a) Fe3 t_{2g} and e_g LDOS and (b), SDTBAT S1, S2 and N1 p-LDOS, before and after adsorption.

The SDTBAT S atoms p-LDOS are shown in Fig. 14b and have reduced states after adsorption which indicated electron loss. The adsorption of SDTBAT S1 atoms resulted in py and pz orbitals largely reduced states, which indicated greater electron loss. From the analysis of the Fe1 and S1 atoms LDOS, it was clear that there was a transfer of electrons from the SDTBAT S1 py and px towards the dyz and dxz orbitals and from the pz towards the dz^2 orbitals. The SDTBAT S2 atom in Fig. 14b clearly showed that the py largely reduced to almost zero states at the VB. This also indicated electron transfer from S2 px and a greater transfer from py towards the dxy orbitals, while the pz transferred towards the dz^2 orbitals of the Fe2 atom. The SDTBAT N1 atom p-LDOS displayed a greater reduction of py and pz to almost zero states at the VB. This indicated that there was a greater hybridisation of the N1 py and pz with Fe3 dyz and dz^2 orbitals, respectively. Interestingly, before adsorption the px was almost at zero states, but after adsorption it had higher states than py and pz orbitals. In all adsorption of the collectors, the S atoms were characterized by large LUMO splitting peak at the CB, while the Fe atoms were characterised by reduced peaks at the CB, which demonstrated electron loss and gain, respectively. In addition the transfer of electrons from the collectors S atoms towards the Fe atoms indicated normal covalent bonding.

In Fig. 15 the charge density difference clearly depict the positive electronic clouds which accept electrons on the bond between the Fe atoms and S and N1 atoms, while the negative electronic clouds which donate electrons was on Fe, S and N1 atoms. This clearly illustrated sharing of electrons/charges and therefore formation of normal covalent bonding and possibly a back-donation covalent bonding of the collector on the pyrite Fe atoms. Table 7 shows the Bader charges in order gain more insights into electron donation and acceptance between the surface Fe atoms and collector S and N1 atoms. In all collector adsorptions, the S atoms adopted less negative charges, while the Fe atoms adopted less positive charges, which indicated charge loss and charge gain, respectively. However, the Fe3 was found to lose charges, with a gain of charges on N1 atom for SDTBAT adsorption. For SNBX adsorption, the

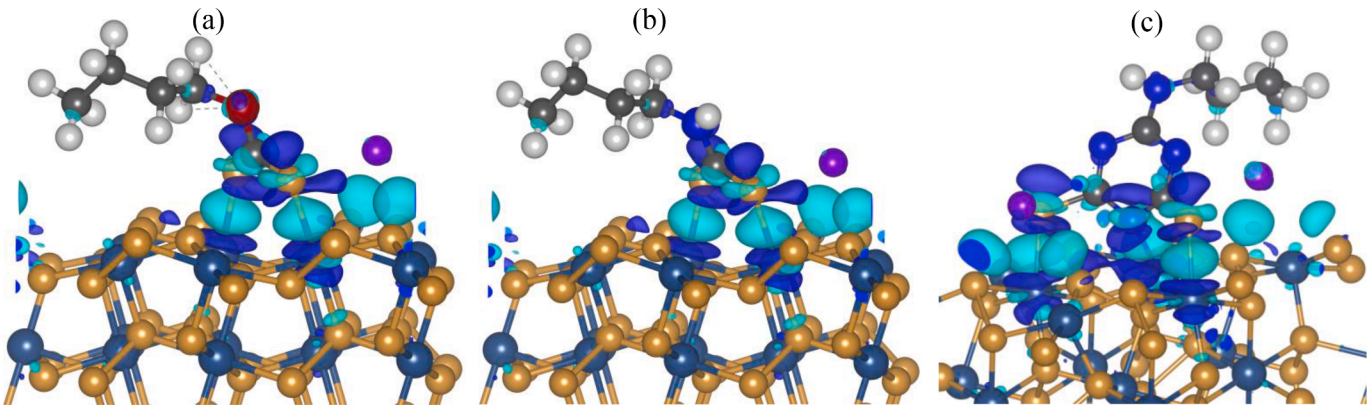

Fig. 15. The sketch of isosurface charge density difference of collector adsorption on pyrite (100) surface: (a) SNBX (isosurface level = 0.003 eÅ^{-3}) and (b) SNBDTC (isosurface level = 0.003 eÅ^{-3}) and (c) SDTBAT (isosurface level = 0.003 eÅ^{-3}). Cyan represents positive electronic clouds which accept electrons and blue stands for negative electronic clouds which donate electrons.

Table 7
Bader charges of SNBX, SNBDTC and SDTBAT collector S atoms and Fe atoms of the FeS_2 (100) surface, before and after adsorption.

		Bader charges (|e$^-$|)		
Adsorption state	Atom	SNBX	SNBDTC	SDTBAT
Before Adsorption	Fe1	+0.66	+0.66	+0.66
After Adsorption	Fe1	+0.65	+0.65	+0.65
Before Adsorption	Fe2	+0.66	+0.66	+0.66
After Adsorption	Fe2	+0.64	+0.64	+0.63
Before Adsorption	Fe3	+0.66	+0.66	+0.66
After Adsorption	Fe3	N/A	N/A	+0.71
Before Adsorption	S1	–0.32	–0.41	–0.36
After Adsorption	S1	–0.08	–0.14	–0.27
Before Adsorption	S2	–0.28	–0.44	–0.41
After Adsorption	S2	–0.21	–0.30	–0.30
Before Adsorption	N1	N/A	N/A	–1.02
After Adsorption	N1	N/A	N/A	–1.11

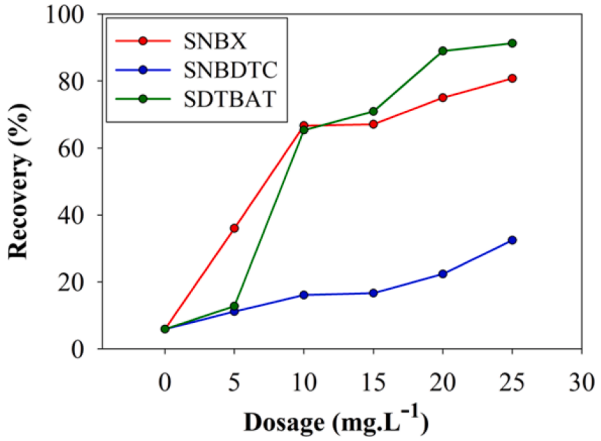

Fig. 16. Micro-flotation recoveries of pyrite at different dosages of SNBX, SNBDTC and SDTBAT collectors.

S1 lost 0.24|e$^-$| and S2 lost 0.07|e$^-$|, while Fe1 gained 0.01|e$^-$| and Fe2 gained 0.02|e$^-$| charges (Table 7). This clearly showed a greater charge loss on the SNBX S1 atom towards Fe1 atom. In the case of SNBDTC adsorption, the S1 lost 0.27|e$^-$| and S2 lost 0.14|e$^-$|, while Fe1 gained 0.01|e$^-$| and Fe2 gained 0.02|e$^-$| charges (Table 7). Also in this adsorption, the SNBDTC S1 lost greater charges towards Fe1 atom.

The adsorption of SDTBAT, depicted that S1 lost 0.09|e$^-$| and S2 lost 0.11|e$^-$| charges, while Fe1 gained 0.01|e$^-$| charges and Fe2 gained 0.03|e$^-$| charges. Furthermore, the N1 atoms gained 0.09|e$^-$| charges, while Fe3 lost 0.05|e$^-$| charges (see Table 7). This showed that the Fe3 atom transferred charge towards N1 atom. The sum of the charges lost on the S atoms, i.e. S1+S2 were found as: 0.31|e$^-$| for SNBX, 0.41|e$^-$| for SNBDTC and 0.20|e$^-$| for SDTBAT. This clearly showed that SNBDTC lost more charges amongst the collectors. The strong binding of SDTBAT on the pyrite surface was ascribed to the charge transfer from the Fe3 atom to the N1 atom. The charges were largely localised on the bond as noted from the charge density difference that the positive electronic clouds which accept electrons was largely on the bond (see Fig. 15). This demonstrated that the collectors adsorb through covalent bonding on pyrite (100) surface.

3.5. Micro-flotation tests

The final recoveries obtained from micro-flotation at different dosages for each collector were calculated according to Eq. (5) as displayed in Table S1 and shown in Fig. 16. The recoveries demonstrated the flotation performance of the SNBX, SNBDTC and SDTBAT collectors for pyrite mineral at the pH = 9.0. The trends of the recoveries were consistent with the predictions based on the computational adsorption energies. Most importantly the green SDTBAT exhibited better flotation performance with high pyrite recoveries of about 70% at 15 mg.L^{-1} dosage and could reach 90% at 20.0 mg.L^{-1} dosage. However, at 5.0 mg.L^{-1} dosage SNBX produced higher pyrite recoveries than SNBDTC and SDTBAT. Significantly, at 10 mg.L^{-1} dosage the SDTBAT increased in recovery to above 60% and almost matched that of SNBX, while that of SNBDTC was around 11% recovery (Fig. 16). This demonstrated that at higher dosages, the SDTBAT surpasses the SNBX in performance. Although the computational adsorption energies and prediction showed that SDTBAT was more reactive and adsorb stronger compared to SNBX on pyrite, the flotation experiment revealed the flotation power of xanthates at low dosages, in particular at dosage of 5.0 mg.L^{-1}. This indicated that in order to validate the computational work, experiments were crucial. The SDTBAT was found to be a better collector than SNBX and SNBDTC as the dosages increases, which is ascribed to the s-triazine group. This suggested that all collectors required higher dosages to float pyrite to above 60%, although SNBDTC performance was poor, with recoveries of up to 32%. This showed that SNBDTC had poor flotation power. The SDTBAT was found to have high flotation power and was proposed as the best collector to compete with the xanthate.

3.6. XPS and FTIR analysis

In order to better understand the adsorption of the SDTBAT collector on pyrite surface, the high-resolution XPS spectra of the pyrite surface

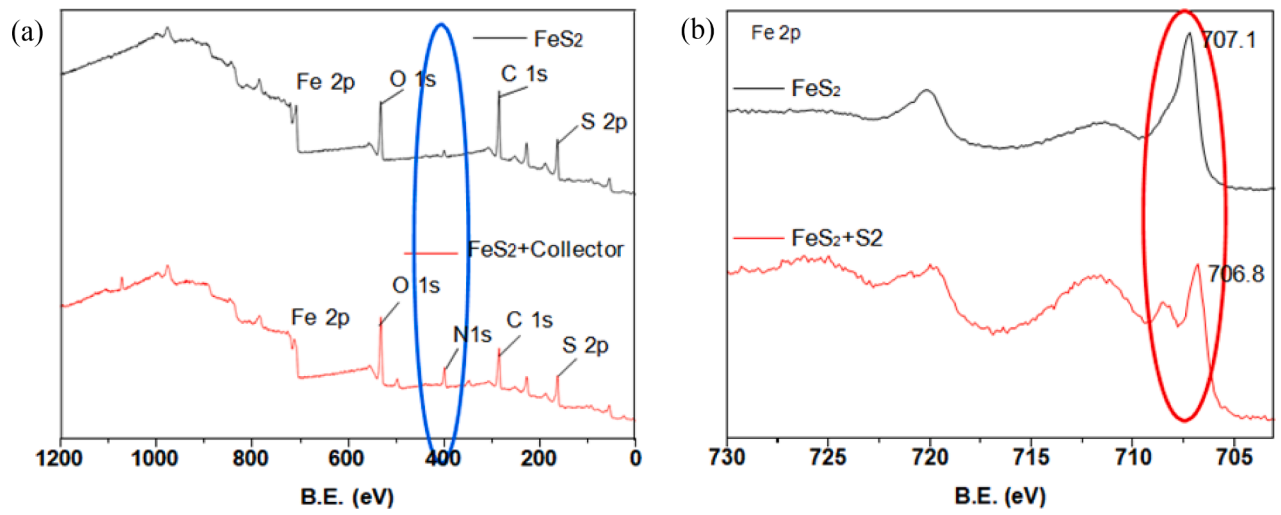

Fig. 17. The XPS analysis of before and after adsorption of SDTBAT collector: (a) Survey XPS spectra of pyrite and (b) High-resolution XPS spectra of Fe 2p.

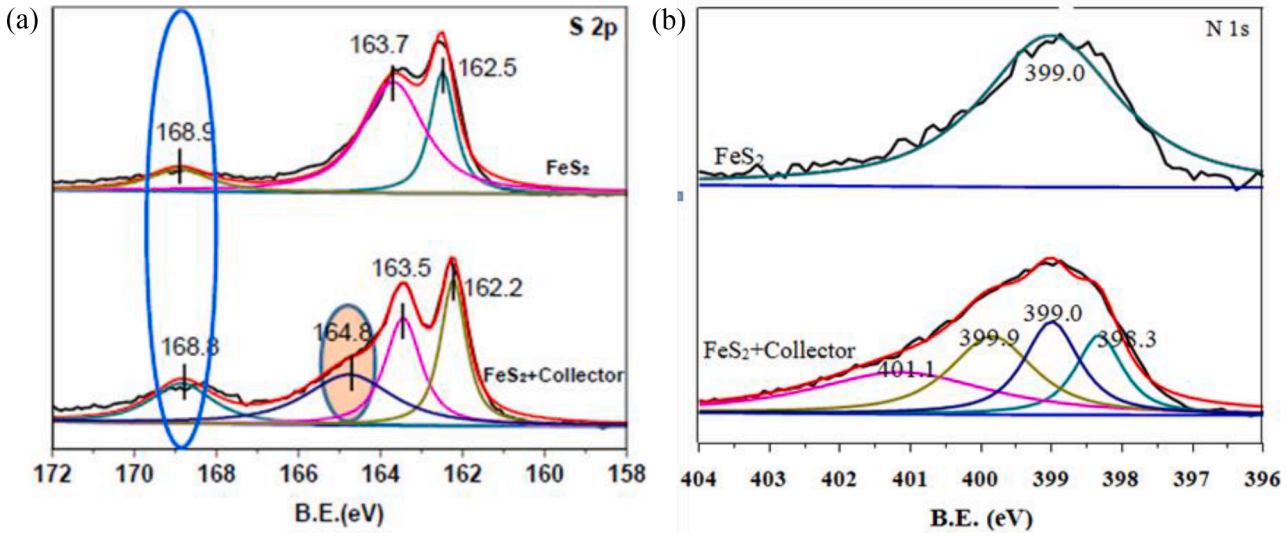

Fig. 18. The high-resolution XPS spectra of before and after adsorption of SDTBAT collector: (a) S 2p and (b) N 1s.

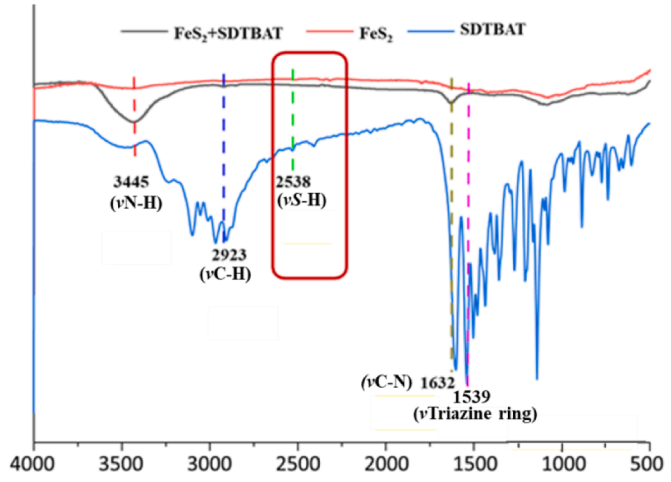

Fig. 19. The FTIR spectra of the SDTBAT collector and pyrite before and after adsorption.

before and after adsorption with SDTBAT were also analysed and of various atoms, among which the spectra of Fe 2p, S 2p and N 1s are shown in Figs. 17–19. An obvious N 1s peak appearing in the XPS spectrum of pyrite after adsorption was noted as shown in Fig. 17a, which indicated that the SDTBAT collector adsorbed on the surface of pyrite owing to a large amount of N elements in SDTBAT collector. Clearly in Fig. 17b, the binding energy of Fe 2p of pyrite moved to the low-energy direction after adsorption, which indicated that after adsorption of the SDTBAT collector, Fe atom accepts electrons from the S atoms of SDTBAT collector. Furthermore, the absorption peak at 1632 cm^{-1} was for C–N stretching vibration, and the absorption peak at 1471 cm^{-1} was for s-triazine characteristic. Meanwhile, the characteristic absorption peak of sulfhydryl group at 2538 cm^{-1} disappeared, which also confirms that the SDTBAT collector chemically bonded with the Fe atom through S and N atoms in collector structure. This resulted in an increase in its electron density and a decrease in its binding energy, thus demonstrating that the SDTBAT collector molecules chemically adsorbed on pyrite surface. Similar bonding behaviour was found from the computational adsorption analysis.

From Fig. 18a, three S 2p peaks (162.5 eV, 163.7 eV and 168.9 eV) were observed in the high-resolution XPS spectra of pyrite before adsorption, of which the first two were from S element in pyrite (162.5

eV, 163.7 eV), while the peak at 168.9 eV was from the oxidized S atoms on pyrite surface. A new S 2p peak at 164.8 eV on pyrite surface after adsorption was noted, which emanated from the S atoms of the SDTBAT collector. However, it retained the characteristics of S atoms peaks on pyrite. These findings proved that the SDTBAT collector adsorbed on pyrite surface.

In Fig. 18b, one N 1s peak at 399.0 eV of pyrite before adsorption was noted and attributed to N_2 pollution during the testing process. The same peak at 399.0 eV still existed after adsorption. Significantly, three new N 1s peaks at 401.1 eV, 399.9 eV and 398.3 eV appeared after the adsorption of SDTBAT collector, which emanated from three kinds of N atoms in the SDTBAT collector molecule (as shown in Fig. 1). This indicated that the SDTBAT collector adsorbed on the pyrite surface.

It was clear in Fig. 19 that after the interaction of pyrite with SDTBAT collector, several obvious characteristic absorption peaks of SDTBAT collector on pyrite surface emerged, which proved that the SDTBAT collector successfully adsorbed on pyrite surface. By comparison of FTIR spectra of pure pyrite and pyrite-collector, it was found that the absorption peak at 3440 cm^{-1} was for N–H stretching vibration, while the absorption peak at 2928 cm^{-1} was for C–H stretching vibration.

4. Conclusions

The s-triazine molecules have not been given much attention and they are potential collectors that may positively impact the mineral processing industry in the separation of sulphide minerals. The computational density functional theory with dispersion correction and *U*-parameter (DFT-D3+*U*) and experimental methods were employed to design and synthesise the green SDTBAT collector for sulphide minerals separations and investigated its adsorption on pyrite mineral surface. The SDTBAT collector was compared with the sodium normal butyl xanthate (SNBX) and sodium normal butyl dithiocarbamate (SNBDTC). The adsorption behaviour of SDTBAT directly related to the reactivity was unravelled using electronic properties, X-ray photoelectron spectroscopy (XPS) and Fourier-transform infrared spectroscopy (FTIR) spectra. Computationally the (100) surface of pyrite was adopted as the most stable surface and experimentally the pure pyrite minerals were used for micro-flotation.

The PDOS and LDOS of the isolated collector showed that the sulphur atoms were more active, with the highest states at E_F, and thus more reactive during adsorption. The reactivity of the collectors prior to adsorptions was determined by the band gaps obtained from the PDOS and it was found that the reactivity order decreased as: SDTBAT > SNBX > SNBDTC. This implied that SDTBAT will be highly reactive and all collectors potentially form covalent bonds and back-donation covalent bonds with sulphide minerals. Computationally, it was observed that the SNBX and SNBDTC adsorbed through the S atoms, while the SDTBAT adsorbed through the S atoms and N atoms onto pyrite Fe atoms. The computational calculated adsorption energies followed the order as: SDTBAT > SNBX > SNBDTC, which predicted that the SDTBAT had strong exothermic adsorption. Moreover, the SDTBAT collector was found to bind stronger than the xanthate. This was complimented by micro-flotation tests that showed fast floating and higher recoveries of pyrite when using the SDTBAT collector that reached 90% as the dosage increases compared to xanthate and DTC.

The LDOS and Bader charges after adsorption showed that the S atoms lose charges to the Fe atoms, while for SDTBAT the N1 gained charges from the Fe3 atom. Interestingly, all collectors S1 atoms lost charges from the py and pz orbitals into the Fe1 dxz, dyz and dz^2 orbitals, while S2 lost from the py, px and pz into the Fe2 dxy and dz^2 orbitals. The case of SDTBAT revealed that N1 gained charges into the py and pz from the Fe3 dyz and dz^2 orbitals. These clearly demonstrated the strong hybridization of the S and N atoms orbitals to form covalent bonding with Fe(II) atoms having $(t_{2g})^6(e_g)^0$ or $(t_{2g})^5(e_g)^1$ on pyrite (100) surface. The XPS and FTIR analysis of pyrite treated and untreated with SDTBAT revealed that the SDTBAT adsorbed through S and N atoms on pyrite Fe sites. In addition, the adsorption of N atoms was noted from the survey scan and XPS data for N 1s. These findings provided a clear correlation between the experiments and DFT-D3+*U* predictions and provided evidence for the adsorption of SDTBAT on Fe sites on the pyrite surface.

The study has shown that the design and modification of green novel collectors such as s-triazine tested on pyrite may be applicable in a wide range of sulphide minerals. This clearly demonstrated that the SDTBAT is a potential collector for sulphide minerals to replace the xanthate collector due to its high flotation power.

CRediT authorship contribution statement

Peace Mkhonto and Xingrong Zhang: Co-wrote the original draft. **Xingrong Zhang and Peace Mkhonto**: Designed the SDTBAT collector. **Peace Mkhonto**: Performed the computational simulations. **Xingrong Zhang, Liang Lu and Xiong Wei:** Synthesized the SDTBAT collector and carried out the micro-flotation tests, XPS and FTIR analysis. **Peace Mkhonto, Xingrong Zhang, Liang Lu, Xiong Wei and Phuti Ngoepe**: Formal analysis of the results. **Peace Mkhonto and Xingrong Zhang:** Conceptualization. **Yangge Zhu, Han Long and Phuti Ngoepe:** Project administration and funding acquisition.

Declaration of Competing Interest

The authors declare that they have no known competing financial interests or personal relationships that could have appeared to influence the work reported in this paper.

Data availability

No data was used for the research described in the article.

Acknowledgments

This work is in collaboration with the Materials Modelling Centre at the University of Limpopo and China-South Africa Joint Research Centre on the Development and Utilization of Mineral Resources and China-South Africa Belt and Road Joint Laboratory on Sustainable Exploration and Utilization of Mineral Resources at BGRIMM Technology Group. Financial support was received from the Department of Science and Innovation (DSI) and National Research Foundation (NRF) of South Africa in the Young Scientist Exchange Program (YSEP) and the National Key R&D Program of China (Grant No. 2020YFE0202800) from Ministry Of Science and Technology (MOST) of China and the National Natural Science Foundation of China (Grant No. 51974030). The computational work benefited from supercomputing resources at the Centre for High Performance Computing (CHPC).

Supplementary materials

Supplementary material associated with this article can be found, in the online version, at doi:10.1016/j.surfin.2023.102820.

References

[1] S.J. Adkins, M.J. Pearse, The influences of collectors chemistry on kinetics and selectivity inbase-metal Sulphide flotation, Miner. Eng. 5 (1992) 295–310.
[2] M. Yekeler, H. Yekeler, A density functional study on the efficencies of 2-mercaptobenzoxazole and its derivatives as chelating agents in flotation processes, Colloids Surf. A Physicochem. Eng. Asp. 186 (2006) 121–125.
[3] B. McFadzean, P. Mkhonto, P.E. Ngoepe, Interactions of xanthates of increasing chain length with pyrite surfaces: a DFT-D and microcalorimetry study, Appl. Surf. Sci. 607 (2023), 154910:1−13.
[4] J.-H. Chen, L.-H. Lan, Y. Chen, Computational simulation of adsorption and thermodynamic study of xanthate, dithiophosphate and dithiocarbamate on galena and pyrite surfaces, Miner. Eng. 46-47 (2013) 136–143.

[5] P.P. Mkhonto, X. Zhang, L. Lu, Y. Zhu, L. Han, P.E. Ngoepe, Unravelling the performance of oxycarbonyl-thiocarbamate collectors on chalcopyrite using first-principles calculations and micro-flotation recoveries, Appl. Surf. Sci. 563 (2021), 150332:1−13.
[6] P.P. Mkhonto, X. Zhang, L. Lu, W. Xiong, Y. Zhu, L. Han, P.E. Ngoepe, Adsorption mechanisms and effects of thiocarbamate collectors in the separation of chalcopyrite from pyrite minerals: DFT and experimental studies, Miner. Eng. 176 (2022), 107318:1–14.
[7] G.S. Maier, B. Dobias, 2-mercaptobenzothiazole and derivatives in the flotation of galena, chalcocite and sphalerite: a study of flotation, adsorption and microcalorimetry, Miner. Eng. 10 (12) (1997) 1375–1393.
[8] Y. Feng, S. Chen, H. Zhang, P. Li, L. Wu, W. Guo, Characterization of iron sulphide modified by 2-mercaptobenzothiazole self-assembled monolayers, Appl. Surf. Sci. 253 (2006) 2812–2819.
[9] T. Jando, K. Mori, Crosslinking of poly(vinyl chloride) fibers with 2-dibutylamino-4,6-dimercapto-1,3,5-triazine in water, Polymer J. 22 (9) (1990) 793–802.
[10] E.-S.A.K. Yacoub, A.-G. El-Kourashy, M.A. Al-Hajjaji, Sorption of iron(II) and ruthenium(III)-triazine complexes on silica gel and its analytical applicability, Arab. J. Chem. 6 (2013) 111–114.
[11] Y.Z. Abdullahi, Y.T. Leong, M.M. Halim, Md.R. Hashim, L.T. Leng, K. Uebayashi, Adsorption of atoms and molecules on s-triazine sheet with embedded manganese atom: first-principles calculations, Phys. Lett. A 381 (2017) 3664–3674.
[12] B. Zhu, S. Wageh, A.A. Al-Ghamdi, S. Yang, Z. Tian, J. Yu, Adsorption of CO2, O2, NO and CO on s-triazine-based g-C3N4 surface, Catal. Today 335 (2019) 117–127.
[13] Y. Benjalal, M.E.A. Ghanjaoui, Theoretical study of di-amino-triazine adsorption on Cu(110) and Au(111) surfaces, J. Mater. Environ. Sci. 7 (5) (2016) 1531–1537.
[14] G. Kresse, J. Hafner, *Ab initio* molecular dynamics for liquid metals, Phys. Rev. B 47 (1993) 558–561.
[15] G. Kresse, J. FurthermÜller, Efficient iterative schemes for *ab-initio* total-energy calculations using a plane-wave basis set, Phys. Rev. B 54 (1996) 11169–11186.
[16] G. Kresse, D. Joubert, From ultrasoft pseudopotentials to the projector augmented-wave method, Phys. Rev. B 59 (1999) 1758–1775.
[17] J.P. Perdew, J.A. Chevary, S.H. Vosko, K.A. Jackson, M.R. Pederson, D.J. Singh, C. Fiolhais, Atoms, molecules, solids, and surfaces: applications of the generalized gradient approximation for exchange and correlation, Phys. Rev. B 46 (1992) 6671–6687.
[18] S.H. Vosko, L. Wilk, M. Nusair, Accurate spin-dependent electron liquid correlation energies for local spin density calculations: a critical analysis, Can. J. Phys. 58 (1980) 1200–1211.
[19] S. Grimme, S. Ehrlich, L. Goerigk, Effect of the damping function in dispersion corrected density functional theory, J. Comput. Chem. 32 (2011) 1456–1465.
[20] H.F. Monkhorst, J.D. Park, Special points for Brillouin-Zone integrations, Phys. Rev. B 13 (1976) 5188–5192.
[21] S.L. Dudarev, G.A. Botton, S.Y. Savrasov, C.J. Humphreys, A.P. Sutton, Electron-energy-loss spectra and the structural stability of nickel oxide: an LSDA+U study, Phys. Rev. B 57 (1998) 1505–1509.
[22] E.C. Dos Santos, M.P. Lourenço, L.G.M. Pettersson, H.A. Duarte, Stability, structure, and electronic properties of the pyrite/arsenopyrite solid−solid interface−A DFT study, J. Phys. Chem. C 121 (2017) 8042–8051.
[23] Y. Li, Y. Liu, J. Chen, C. Zhao, W. Cui, Comparison study of crystal and electronic structures for chalcopyrite (CuFeS2) and pyrite (FeS2), Physicochem. Probl. Miner. Process. 57 (1) (2021) 100–111.
[24] H. Xian, X. Wu, J. Zhu, R. Du, J. Wei, R. Zhu, H. He, Environmental sulfur controlled surface properties of pyrite: a first principles PBE+U study, Phys. Chem. Miner. 48 (20) (2021) 1–11.
[25] A. Ennaoui, S. Fiechter, Ch. Pettenkofer, N. Alonso-Vante, K. Büker, M. Bronold, Ch. Höpfner, H. Tributsch, Iron disulfide for solar energy conversion, Sol. Energy Mater. Sol. Cells 29 (1993) 289–370.
[26] A. Ennaoui, H. Tributsch, Energetic characterization of the photoactive FeS2 (pyrite) interface, Sol. Energy Mater. Sol. Cells 14 (6) (1986) 461–474.
[27] H. Choi, J.Y. Seo, Y.R. Uhm, G.M. Sun, C.S. Kim, Crystalline structure and magnetic properties of pyrite FeS2, AIP Adv. 11 (2021), 015131, 1-5.
[28] T.L.P. Galvao, A. Kuznetsova, J.R.B. Gomes, M.L. Zheludkevich, J. Tedim, M.G. S. Ferreira, A computational UV-Vis spectroscopic study of the chemical speciation of 2-mercaptobenzothiozole corrosion inhibitor in aqueous solution, Theor. Chem. Acc. 135 (78) (2016) 1–11.
[29] E. Sanville, S.D. Kenny, R. Smith, G. Henkelman, An improved grid-based algorithm for Bader charge allocation, J. Comput. Chem. 28 (2007) 899–908.
[30] G. Henkelman, A. Arnaldsson, H. Jonsson, A fast and robust algorithm for Bader decomposition of charge density, Comput. Mater. Sci. 36 (2006) 354–360.
[31] R.F.W. Bader, Atoms in Molecules: A Quantum Theory, Oxford University Press, London, UK, 1994.
[32] P.P. Mkhonto, H.R. Chauke, P.E. Ngoepe, Ab-initio studies of O2 adsorption on (110) nickel-rich pentlandite (Fe4Ni5S8) mineral surface, Miner 15 (2015) 1195–1198.
[33] K. Momma, F. Izumi, VESTA: A three-dimensional visualization system for electronic and structural analysis, J. Appl. Crystallogr. 41 (2008) 653–658.
[34] P.P. Mkhonto, P.E. Ngoepe, Reconstruction of cooperite (PtS) surfaces: a DFT-D+U study, ACS Omega (2022), https://doi.org/10.1021/acsomega.2c02867.
[35] B. Nemutudi, P.P. Mkhonto, P.E. Ngoepe, Oxidation behaviour of sperrylite and platarsite (100) surfaces: A DFT study, Mater. Today Commun. 32 (2022), 103868: 1−11.
[36] X. Tian, T. Wang, L. Fan, Y. Wang, H. Lu, Y. Mu, A DFT based method for calculating the surface energies of asymmetric MoP facets, Appl. Surf. Sci. 427 (2018) 357–362.
[37] K.M. Rosso, U. Becker, M.F. Hochella Jr., Atomically resolved electronic structure of pyrite {100} surfaces: An experimental and theoretical investigation with implications for reactivity, Am. Mineral. 84 (1999) 1535–1548.
[38] J. Chen, The interaction of flotation reagents with metal ions in mineral surfaces: a perspective from coordination chemistry, Min. Eng. 171 (2021), 107067:1-15.
[39] M. Bronold, Y. Tomm, W. Jaegermann, Surface states on cubic d-band semiconductor pyrite (FeS2), Surf. Sci. Lett. 314 (1994) L931–L936.
[40] G. Klopman, Chemical reactivity and the concept of charge- and frontier-controlled reactions, J. Am. Chem. Soc. 90 (1968) 223–230.
[41] G.-Y. Liu, H. Zhong, T. Dai, L.-Y. Xia, Investigation of the effect of N-substituents on performance of thionocarbamates as selective collectors for copper sulfides by ab initio calculations, Miner. Eng. 21 (2008) 1050–1054.